

# Enhanced bone regenerative properties of calcium phosphate ceramic granules in rabbit posterolateral spinal fusion through a reduction of grain size

Xiangfeng Li<sup>a</sup>, Quan Zhou<sup>b</sup>, Yonghao Wu<sup>a</sup>, Cong Feng<sup>a</sup>, Xi Yang<sup>b</sup>, Linnan Wang<sup>b</sup>, Yumei Xiao<sup>a</sup>, Kai Zhang<sup>a</sup>, Xiangdong Zhu<sup>a,\*</sup>, Limin Liu<sup>b</sup>, Yueming Song<sup>b,\*\*</sup>, Xingdong Zhang<sup>a</sup>

<sup>a</sup> National Engineering Research Center for Biomaterials, College of Biomedical Engineering, Sichuan University, Chengdu, 610064, China

<sup>b</sup> Department of Orthopaedic Surgery, West China Hospital of Sichuan University, Chengdu, 610041, China

## ARTICLE INFO

### Keywords:

Calcium phosphate ceramics  
Nanotopography  
Osteogenic differentiation  
Osteoinductivity  
Posterolateral spinal fusion

## ABSTRACT

Osteoinductivity is a crucial factor to determine the success and efficiency of posterolateral spinal fusion (PLF) by employing calcium phosphate (Ca-P) bioceramics. In this study, three kinds of Ca-P ceramics with microscale to nanoscale grain size (BCP-control, BCP-micro and BCP-nano) were prepared and their physicochemical properties were characterized. BCP-nano had the spherical shape and nanoscale grain size, BCP-micro had the spherical shape and microscale grain size, and BCP-control (BAM®) had the irregular shape and microscale grain size. The obtained BCP-nano with specific nanotopography could well regulate *in vitro* protein adsorption and osteogenic differentiation of MC3T3 cells. *In vivo* rabbit PLF procedures further confirmed that nanotopography of BCP-nano might be responsible for the stronger bone regenerative ability comparing with BCP-micro and BCP-control. Collectively, due to nanocrystal similarity with natural bone apatite, BCP-nano has excellent efficacy in guiding bone regeneration of PLF, and holds great potentials to become an alternative to standard bone grafts for future clinical applications.

## 1. Introduction

Posterolateral spinal fusion (PLF) is a common procedure in orthopedic surgery to treat spinal instability caused by spinal trauma, degenerative conditions, scoliosis or tumor resections [1–3]. Apart from fixation systems such as rods, plates and screws, the procedure generally requires bone grafting to further reinforce the spinal fusion [2,4]. Traditionally, autogenous grafts from the iliac crest are considered as the gold standard for achieving successful spinal fusion. Still, the limited supply, donor site morbidity, chronic pain and bone resorption restrict their wide applications in the clinic [5–7]. For PLF surgery, the procedure generally requires large volume of bone graft, about 12–36 mL, which is a relatively large amount for autogenous grafts from the iliac crest [8,9]. Allografts are attractive alternatives to autografts, but they are doubted by the risk of potential disease transmission and immunogenicity [2]. In order to accelerate the fusion rate of PLF procedures and to reduce the amount of autografts to be harvested, a variety of artificial

grafts have been proposed for spine fusion in animal models or clinical applications, such as demineralized bone matrix, bioactive glass, silicate substitutes, calcium phosphate (Ca-P) bioceramics and etc. [10,11].

The osteogenic environment around posterolateral spine is known to be challenging for bone grafts because of the limited contact with host bone and the long bone crawling distance. Even for the gold standard grafts of autologous bone, pseudoarthrosis and non-unions are still frequently reported due to the complications of this treatment [3,12,13]. Therefore, the development of artificial grafts with high bone regenerative ability is the fundamental way to treat this intractable disease. Among the various kinds of artificial grafts, Ca-P bioceramics were undoubtedly one of the most important biomaterials, due to their similarity in bony mineral, good biocompatibility, bioactivity, osteoconductivity and so on [1,14]. More importantly, biphasic calcium phosphate (BCP) bioceramics with specific phase composition (a certain HA/ $\beta$ -TCP phase ratio) and pore structure could be endowed with good osteoinductivity, which could induce the mesenchymal cells to differentiate along the

Peer review under responsibility of KeAi Communications Co., Ltd.

\* Corresponding author.

\*\* Corresponding author.

E-mail addresses: [zhu\\_xd1973@scu.edu.cn](mailto:zhu_xd1973@scu.edu.cn) (X. Zhu), [sym\\_cd@163.com](mailto:sym_cd@163.com) (Y. Song).

<https://doi.org/10.1016/j.bioactmat.2021.10.006>

Received 15 June 2021; Received in revised form 2 October 2021; Accepted 3 October 2021

Available online 8 October 2021

2452-199X/© 2021 The Authors. Publishing services by Elsevier B.V. on behalf of KeAi Communications Co. Ltd. This is an open access article under the CC

BY-NC-ND license (<http://creativecommons.org/licenses/by-nc-nd/4.0/>).

osteogenic lineage, and ultimately to form new bone [15–17]. The most striking feature of osteoinductivity is that biomaterials can induce the new bone formation ectopically without adding any growth factors or cells, even in muscle or under the skin, which brings hopes to regenerate some complex bone defects, such as large-size bone defect, segmental bone defect and other weakly osteogenic environments [15,16,18]. However, present Ca-P bioceramics still cannot meet the needs of regenerative medicine, such as limited bioactivity, dissatisfied osteoinductivity, unsuitable biodegradability and so on [19].

To the best of our knowledge, the optimal approach to fabricating bone repairing scaffolds is biomimetics. It is well established that the natural bone is mainly composed of hydroxyapatite nanocrystals and collagen fibers [20,21]. However, the conventional Ca-P bioceramics, despite mimicking the phase composition and porous structure in part, have the large grain size at the microscale. The relatively large grain size is certain to debase the bioactivity, biodegradability, osteoinductivity, even bone regenerative ability of Ca-P bioceramics. Luckily, present progress in nanotechnology allows us to fabricate Ca-P nanoceramics [22–24]. In our previous works, Ca-P nanoceramics with the grain size of about 100 nm were successfully fabricated by a novel microwave hybrid sintering method [25–27]. Comparing with Ca-P microceramics, Ca-P nanoceramics have many advantages [16,26,28]. 1) Unique surface topography: nanoceramics possess high specific surface area and abundant micropores, which are favorable for protein adsorption and deposition of bone-like apatite nanocrystals. 2) Good bioactivity: nanoceramics could well initiate and regulate a cascade of gene activities of cells, especially for osteogenic differentiation. 3) Excellent osteoinductivity: either for osteogenic occurrence time or osteogenesis quality, nanoceramics have significant advantages. 4) Proper biodegradability: the nanocrystal could enhance the biodegradability of Ca-P bioceramics, which is usually too low, and the dissolving  $\text{Ca}^{2+}$  and  $\text{PO}_4^{3-}$  are indispensable inorganic components in bone formation. These desirable properties are bond to enhance the bone regenerative ability of Ca-P bioceramics, and widen their clinic applications. Still, the biological risk of Ca-P nanoceramics cannot be ignored. Due to the faster degradation rate, the nanoparticles degraded from Ca-P nanoceramics may enter into cells or blood to cause the potential risks [16]. So, the biological performances and the potential threats of Ca-P nanoceramics should be systematically investigated before clinical applications.

Based on the above descriptions, the study herein attempts to develop the porous BCP nanoceramic spheres and evaluate their bone regenerative abilities in a rabbit PLF model (Scheme 1). Porous BCP ceramic spheres with microscale grain size and commercial BCP

granules (BAM®) were used as control groups. Their physicochemical properties, included morphology, grain size and pore structure, were firstly characterized. Then, *in vitro* cellular biocompatibilities of MC3T3E-1 on the three groups were evaluated, and their abilities to induce osteogenic differentiation were further compared. Finally, their ability of inducing bone regeneration was assessed utilizing a PLF model in rabbits.

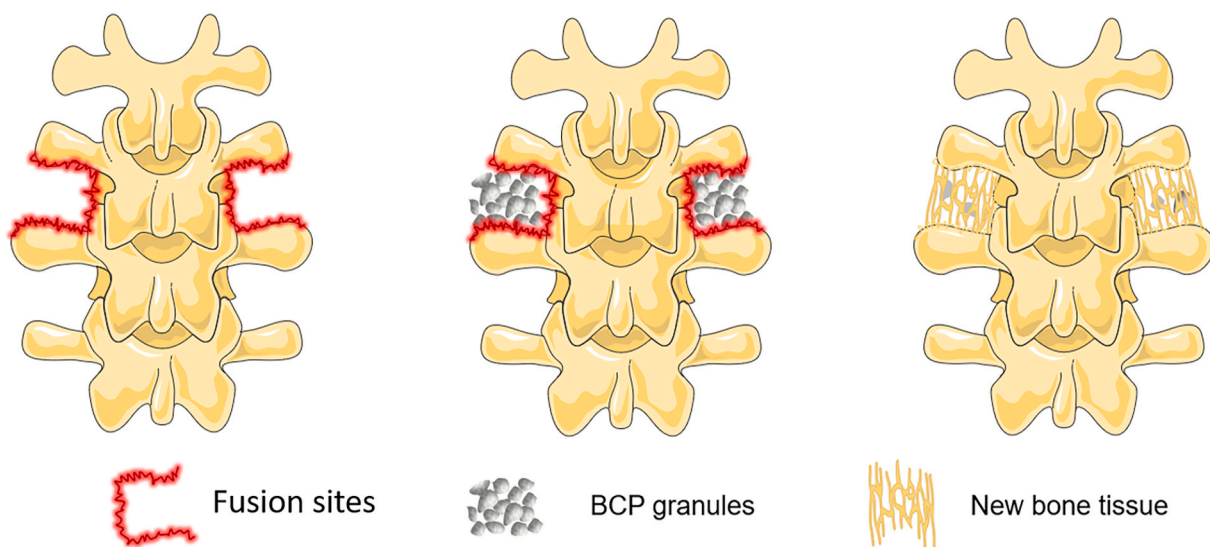
## 2. Materials and method

### 2.1. Material preparation

The spherical BCP ceramic granules were fabricated by an alginate-gelatinizing method, as reported in our previous work [26,29]. In brief, BCP powder (10 g, provided by National Engineering Research Center for Biomaterials, Sichuan University) with the phase ratio of HA/ $\beta$ -TCP of 2:8 was uniformly dispersed in the 25 mL sodium alginate solution (6 wt%, CAS: 9005-38-3, Sigma-Aldrich, USA) by a homogenizer (T10 basic ULTRA-TURRAX, IKA, Germany). Then the bubbly slurry produced by the  $\text{H}_2\text{O}_2$  forming method was extruded into  $0.45 \text{ mol L}^{-1}$   $\text{CaCl}_2$  (CAS: 10043-52-4, Chengdu Chron Chemicals Co., Ltd, China) solution to form the spherical gel granules. After hardening and drying, the granules were separately sintered by conventional muffle sintering ( $1050^\circ\text{C}$  for 2 h) and microwave sintering ( $1050^\circ\text{C}$  for 5min) to obtain BCP ceramic granules with microscale to nanoscale grain size. The samples sintered by conventional muffle sintering were denoted as BCP-micro, and the samples sintered by microwave sintering were denoted as BCP-nano. For comparison, the commercially irregular BCP ceramic granules (BAM® P2040, produced by Sichuan BAM Bioactive Materials Limited Liability Company) were used as the control group, which were fabricated by crushing Ca-P porous bioceramic blocks, and denoted as BCP-control. The osteoinductivity of BCP-control has certified in our previous work [26]. Prior to use, the samples were sterilized by G-ray irradiation (25–30 kGy) to avoid altering their physicochemical properties.

### 2.2. Material characterization

The microstructures and grain sizes of the obtained samples were observed by a scanning electron microscopy (SEM; JSE-5900LV, Japan). The crystalline phases of HA (09-0432) and  $\beta$ -TCP (09-0169) in the BCP ceramics were determined by X-ray diffractometry (XRD; Philips X'Pert 1 X-ray diffractometer, Netherlands) with  $\text{Cu K}\alpha$  radiation at a current of 20 mA and voltage of 30 kV. Their porosity, microporosity and pore



**Scheme 1.** The process of bone generation in posterolateral spinal fusion by employing osteoinductive BCP ceramic granules.

structure were tested by a mercury porosimetry (AutoPore IV 9500, Micromeritics). A surface area analyzer (Gemini VII 2390t, Micromeritics) was employed to test the specific surface area (SSA) of the samples. Moreover, the concentrations of  $\text{Ca}^{2+}$  and  $\text{PO}_4^{3-}$  releasing from the samples were characterized by an inductively coupled plasma optical emission spectrometer (SPECTRO ARCOS).

### 2.3. Protein adsorption

To assess the protein adsorbing abilities of the obtained BCP granules, bovine serum albumin (BSA, GIBCO, USA) and fibronectin (FN, GIBCO, USA) were employed as the targeted protein. A certain quality of samples was firstly placed into the 24-well plates, completely wetted by PBS, and then 1 mL of protein per well was added. After incubating at 37 °C for 4 h, the adsorbed proteins on the samples were eluted by 2% sodium dodecyl sulfonate (SDS) solution and analyzed by BCA™ protein assay kit (Pierce, USA). The detailed process could be found in our previous work [29].

### 2.4. Calcium and phosphate concentrations in the media

$\alpha$ -minimum essential medium ( $\alpha$ -MEM, Gibco, NY, USA) was employed to evaluate the  $\text{Ca}^{2+}$  and  $\text{PO}_4^{3-}$  ions releasing abilities of the obtained BCP granules. The samples were immersed in  $\alpha$ -MEM solution with a solid-liquid ratio of 1:100 in a thermostatic oscillator (37 °C, 2 Hz). At each time point (0.5, 1, 2, 3, 5, 7 d), 0.5 mL of the immersed solution was taken out to measure the  $\text{Ca}^{2+}$  and  $\text{PO}_4^{3-}$  concentrations, and the same volume of fresh  $\alpha$ -MEM was added.

## 2.5. Cellular behavior

### 2.5.1. Cell culture

The murine MC3T3-E1 pre-osteoblasts were selected as the cell model to evaluate the cytocompatibility and osteogenic activity of the obtained BCP granules. The cells were cultured in  $\alpha$ -minimum essential medium ( $\alpha$ -MEM, Gibco, NY, USA) containing 10% fetal bovine serum (FBS, Gibco), 100 U mL<sup>-1</sup> penicillin and 100 mg mL<sup>-1</sup> streptomycin. The medium was renewed every two days.

### 2.5.2. Cell spreading and proliferation

MC3T3-E1 were trypsinized and seeded on the sterilized samples in 48-well plates (Corning, PA) with a density of  $1 \times 10^4$  cells per well. used to evaluate the attachment and growth of the cells on the samples. After culturing for 1, 3 and 5 days, the attached cells on the samples were stained with  $2 \times 10^{-6}$  mol L<sup>-1</sup> Calcein-AM and  $4.5 \times 10^{-6}$  mol L<sup>-1</sup> propidium iodide (PI, Solarbio, China) and then visualized by a confocal laser scanning microscopy (CLSM; TCSSP5, Leica, Germany). Moreover, cell proliferation was quantified by MTT assay. In order to visualize cell spreading, the attached MC3T3 were also observed by SEM, which dehydrated through gradient ethanol solution and dried by a critical-point drier (HCP-2, Hitachi, Japan). In addition, the fixed samples were also stained with TRITC conjugated-phalloidin (1: 200, Sigma, USA) for cytoskeletal protein (F-actin) and DAPI (1: 1000, Sigma, USA) for cell nuclei, and then examined under a CLSM.

### 2.5.3. ALP activity and alizarin red-S staining

MC3T3 were firstly seeded in 24-well plates with a density  $1 \times 10^4$  cells and incubated for 12 h to allow cell adhesion. Subsequently, BCP granules were placed in Millicell filter inserts with diameter of 12 mm and pore size of 8  $\mu\text{m}$  (Millipore, Billerica, MDUSA) to avoid direct contact with the cells [30]. After culturing for 4 and 7 days, ALP staining was carried out according to the specifications (Beyotime, China). In addition, ALP activity was further quantified by a pNPP Alkaline Phosphatase Assay Kit (Sensolyte, USA), and the total protein content was assessed by a BCA protein assay kit (Thermo Scientific, USA). To investigate the mineralization of the MC3T3 culturing with the obtained

samples, Alizarin Red S (Alfa Aesar, USA) was conducted according to the manufacturer's procedures. To quantify the calcium nodule, the stain was desorbed with 10% hexadecylpyridinium chloride solution (Sigma-Aldrich, St. Louis, Mo. USA) for 1 h, the absorbance of the dissolved solution was determined at 630 nm.

### 2.5.4. Immunofluorescent staining

After culturing for 14 days, MC3T3 cultured on the samples were fixed. Immunofluorescent staining of several osteogenic markers was performed, and rabbit anti-bone morphogenetic protein 2 (anti-BMP-2) primary antibody (1:50, Novus, USA), rabbit anti-Runx-2 primary antibody (1:1000, Abcam, UK), rabbit anti-collagen-I (anti-COL-I) primary antibody (1:200, Abcam, UK), rabbit anti-osteocalcin (anti-OCN) primary antibody (1:400, Abcam, UK), rabbit anti-osteopontin (anti-OPN) primary antibody (1:50, Novus, USA), and FITC-conjugated goat anti-rabbit secondary antibody (Alexa Fluor®488 & Fluor®594, USA) were employed. And cell nuclei were stained with DAPI (1: 1000, Sigma) and examined under a CLSM. For BMP-2, Runx-2, COL-I and OCN, the target protein was stained by red fluorescent, the cytoskeleton was stained by green fluorescent, and the cell nucleus was stained by red fluorescent. For OPN, the target protein was stained by green fluorescent, the cytoskeleton was stained by red fluorescent, and the cell nucleus was stained by red fluorescent.

### 2.5.5. Osteogenic gene expressions

The osteogenic gene expressions of MC3T3 stimulated by BCP granules were analyzed using real-time quantitative reverse transcription PCR reaction (qRT-PCR). At day 4, 7 and 14, the total RNA of culturing cells was extracted with a Rneasy Mini Kit (BIO-RAD, USA) and reverse-transcribed into complementary DNA (cDNA) by an iScript cDNA Synthesis Kit (BIO-RAD, USA). Then, gene expressions were verified via quantitative PCR using SoFast™ EvaGreen® Supermix kit (Bio-Rad, USA) on a CFX96™ real-time PCR detection system. A series of osteogenic genes, including runt-related transcription factor 2 (*Runx2*), alkaline phosphatase (*Alp*), collagen I (*Col-1*), osterix (*Osx*), Osteocalcin (*Ocn*) and osteopontin (*Opn*) were characterized. And  $\beta$ -actin was used as a housekeeping gene. The relative gene expression levels were analyzed by the  $\Delta\Delta\text{Ct}$ -value method. The sequences of all primers were listed in Table S1.

### 2.5.6. Western blotting

For the Western blot analysis, MC3T3 cells cultured on samples for 14 days were harvested. Then, the cells were collected and lysed with RIPA lysis buffer (Cowin Biotech, Beijing, China). Similar to our previous work [31], the total cell lysate was separated by polyacrylamide gel electrophoresis (PAGE) and electro-transferred to PVDF membranes Hybond-P (GE Health Sciences, Piscataway, NJ). After incubating in 5% dried nonfat milk for 45 min, the membranes were blocked and incubated with appropriate primary antibodies including COL-I, BSP, OPN, OCN, (diluted 1:1000; Cell Signaling, MA, USA) at 4 °C overnight. Finally, the membranes were visualized with horseradish peroxidase (HRP) conjugated secondary antibody (diluted 1:5000; Santa Cruz, CA, USA) at 37 °C for 1 h using enhanced chemiluminescence (ECL) detection method. Relative protein levels were normalized against  $\beta$ -actin. Quantitative densitometric analysis of the images was carried out using ImageJ software.

## 2.6. Animal experiment

### 2.6.1. Operative procedure

The animal experiment was approved by the Institutional Animal Care and Use Committee (IACUC) of Sichuan University. A total of 24 adult female New Zealand white rabbits (3-4 months old, about 2.5 kg) underwent bilateral PLF process at L5-L6 spine arthrodesis. The animals were anesthetized with sodium pentobarbital (1 mg kg<sup>-1</sup>). Firstly, a midline incision was made in the skin, and the intermuscular plane

between the multifidus and longissimus muscles was bluntly incised to expose the L5 and L6 transverse processes. Then, a high-speed burr was used to decorticate the transverse processes with a uniform manner in all rabbits. Due to the bilateral PLF process, there were totally 48 implanting sites. The groups were divided into three groups, BCP-micro ( $n = 16$ ), BCP-nano ( $n = 16$ ) and BCP-control ( $n = 16$ ). A total of 3 mL of ceramic granules were implanted over the decorticated transverse region per side, and one rabbit received the same ceramic granules for the bilateral PLF process. Subsequently, the muscle and skin were sutured in layers. The detailed surgery procedure was illustrated in Fig. S2. After surgery, each rabbit received gentamicin ( $20000 \text{ U kg}^{-1}$ ) daily through intramuscular injection for three consecutive days. After implanting for 90 days, the rabbits were sacrificed by lethal intravenous injection of sodium pentobarbital.

### 2.6.2. X-ray evaluation and manual palpation

After harvest, X-rays (630 mA X-ray, Shimadzu, Japan) were carried out after implanting for 45 days (intravital analysis) and 90 days (excised analysis). Since BCP ceramics are not X-ray permeable, X-rays were scored according to the criteria described by Lopez MJ et al., 0 score represents no signs of new bone formation; 1 score represents a few new bones formed but not fused; 2 score represents immature bone formation and suspected fusion; 3 score means possible solid integration [32]. Moreover, the stability of the spines was assessed by manual palpation immediately [33,34]. The treated motion segments in lateral bending and flexion/extension were assessed comparing with the proximal and distal motion segments, and both sides of each sample were scored separately. The fusion area was graded as either fused (rigid, 1 point) or no fused (no rigid, 0 point), and there were 2 points in total for each animal. Fusion was considered if the intervertebral movement was not touched by the surgical segment fixation; otherwise, it was considered non-fusion. Two trained and experienced observers who were blinded for the treatment assessed the X-ray evaluation and manual palpation.

### 2.6.3. Micro-CT measurement

Micro-CT (CT80, Scanco Medical AG, Switzerland) was employed to further assess the bone regeneration of PLF with a resolution of  $22 \mu\text{m}$ , the tube voltage was 70 kV and the tube current was  $114 \mu\text{A}$ . A global threshold was applied to distinguish materials from the mineralized bone tissue according to our previous work [35,36]. The obtained images were reconstructed, and the bone mineral density (BMD) and bone volume fraction (BV/TV) of samples after implantation were analyzed using Scanco software according to our previous work [26].

### 2.6.4. Sequential fluorescent labeling

The sequential fluorescent labeling of mineralizing process in the defects was carried out according to the previous report [37]. After operation for 8 weeks, the rabbits were subjected to intraperitoneal injection of tetracycline hydrochloride (TE, Sigma-Aldrich, St. Louis, Mo. USA) following the dozen of  $1 \text{ mg kg}^{-1}$  body weight. After operation for 10 weeks, the rabbits were subsequently subjected to intraperitoneal injection of calcein (CA, 1% in 2%  $\text{NaHCO}_3$  solution, Sigma-Aldrich, St. Louis, Mo. USA) following the dozen of  $5 \text{ mL kg}^{-1}$  body weight.

### 2.6.5. Biomechanical analysis

Only the bilaterally fused samples (three of the fused spines from each group) were randomly selected to perform biomechanical analysis. The samples were stored in a refrigerator at  $-80^\circ\text{C}$ , and each of them was utterly thawed at room temperature before biomechanical testing. A universal mechanics tester (Instron 5967, America) was employed to carry out three-point bending testing of the specimens [6,38]. Briefly, the L5-L6 segments were placed above the two jigs with a width of 25 mm, and the force was loaded on the ventral surface of the intervertebral disc, which was vertical to the longitudinal spine. A compression force was applied at a constant displacement speed of  $0.5 \text{ mm min}^{-1}$  until

fractured. Load and displacement were recorded, and the maximum bending load, maximum bending load and bending stress were calculated.

### 2.6.6. Histological analysis

The hard-tissue slide method was employed to perform the histological analyses, the remaining fused specimens were analyzed. Briefly, the tissue was firstly fixed in 4% paraformaldehyde and dehydrated by gradient alcohol, then embedded in polymethylmethacrylate (PMMA). The sections were cut and polished to  $10\text{--}30 \mu\text{m}$  by a microtome (EXAKT 300, Germany) and stained with methylene blue and basic fuchsin. The stained sections were scanned using a digital scanner (BA600, Motic China Group Co., Ltd.), and the quantitative analysis of bone area percentage were analyzed by Image-Pro Plus (IPP, Media Cybernetic) 6.0 software.

### 2.7. Statistical analysis

All data are presented as mean  $\pm$  standard deviation. At least three samples were used for each data point. One-way analysis of variance (ANOVA) followed by a Tukey's post hoc test was used in experiments with three groups, and two-way ANOVA followed by Tukey's multiple comparisons test was used in experiments with three groups at different time points. Statistical analysis was carried out using the GraphPad Prism statistical program (GraphPad Software Inc, La Jolla, CA, USA). The difference was considered statistically significant at a  $P$  value  $< 0.05$ .

## 3. Results

### 3.1. Physicochemical characterization

The morphologies of the obtained three kinds of BCP ceramic granules were shown in Fig. 1A, BCP-micro and BCP-nano exhibited well spherical shape with the diameter of about 2  $\mu\text{m}$ , while BCP-control had a random irregular shape with the size of 2–4  $\mu\text{m}$ . Moreover, their grain size was different (Fig. 1B), BCP-control had the largest grain size of  $652.9 \pm 153.9 \text{ nm}$  (list in Table 1), followed by BCP-micro of  $503.9 \pm 105.6 \text{ nm}$ , BCP-nano had the smallest one of  $122.8 \pm 30.1 \text{ nm}$ , which was in nanoscale. The pore size distribution and pore quantity distribution of BCP-micro, BCP-nano and BCP-control were compared in Fig. 1C, the three groups possessed a similar macropores distribution of 200–800  $\mu\text{m}$  and interconnected pores distribution of 10–100  $\mu\text{m}$ . From pore size distributions, the number of micropores (20–200 nm) in BCP-nano was significantly higher than those in BCP-micro and BCP-control. All the three kinds of BCP granules had relatively high porosities (70–80%, list in Table 1), but the microporosity ( $<10 \mu\text{m}$ ) of BCP-nano ( $33.29 \pm 2.67\%$ ) was higher than BCP-micro ( $23.67 \pm 1.05\%$ ) and BCP-control ( $18.51 \pm 1.69\%$ ). Moreover, the specific surface area (SSA) of BCP-nano ( $6.656 \pm 1.406 \text{ m}^2 \text{ g}^{-1}$ , list in Table 1) was also larger than BCP-micro ( $0.850 \pm 0.054 \text{ m}^2 \text{ g}^{-1}$ ) and BCP-control ( $0.594 \pm 0.146 \text{ m}^2 \text{ g}^{-1}$ ), and BCP-control had the smallest SSA among the three groups.

The comparisons of XRD patterns of BCP-micro, BCP-nano and BCP-control were exhibited in Fig. 1D. All of them were only composed of  $\beta$ -TCP phase and HA phase from determining their diffraction peaks. By calculating, the contents of HA phase in BCP-micro and BCP-nano were higher than BCP-control (list in Table 1), indicated that the alginate gelation method could increase the HA phase ratio in BCP-micro and BCP-nano [39]. Fig. 1E exhibited the  $\text{Ca}^{2+}$  and  $\text{PO}_4^{3-}$  releasing abilities of the three groups in  $\alpha$ -MEM solution. From  $\text{Ca}^{2+}$  releasing curves, the  $\text{Ca}^{2+}$  concentrations releasing from BCP granules increased firstly (0–0.5 day), then decreased (0.5–7 day). But the decreasing extents of the three groups were different, BCP-micro and BCP-nano had the relatively higher decreases of  $\text{Ca}^{2+}$  concentrations than BCP-control. Similar decreases were also observed in the  $\text{PO}_4^{3-}$  releasing curves, the decreases of  $\text{Ca}^{2+}$  concentrations in BCP-micro and BCP-nano were also higher

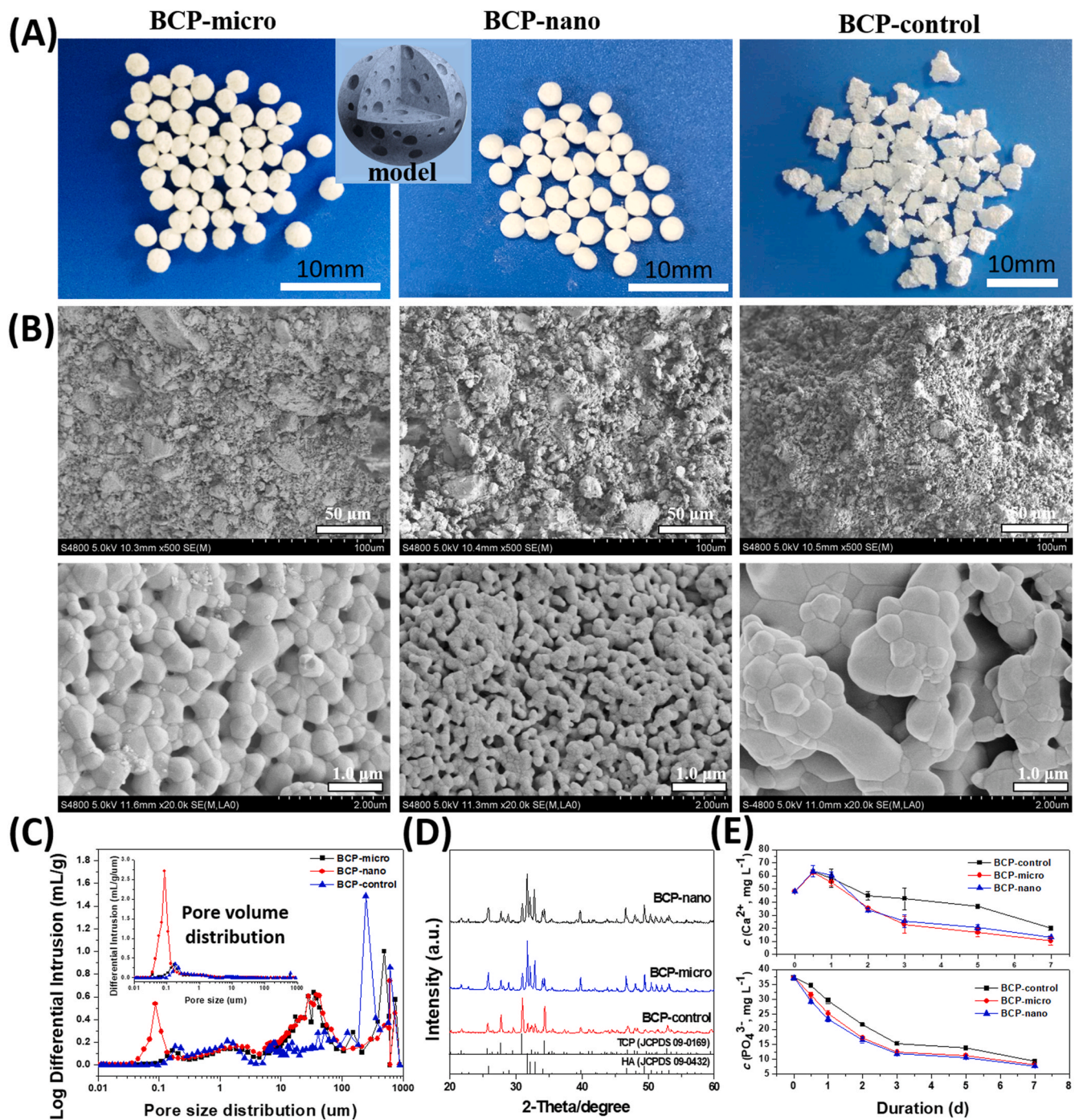


Fig. 1. (A) Model and morphologies, (B) SEM images, (C) pore size distributions and pore quantity distributions, (D) XRD patterns and (E) Ca<sup>2+</sup> and PO<sub>4</sub><sup>3-</sup> releasing abilities in α-MEM solution of BCP-micro, BCP-nano and BCP-control.

than that in BCP-control. These results indicated that BCP-micro and BCP-nano facilitate the precipitation of apatite on their surfaces comparing with BCP-control.

### 3.2. Protein adsorption and cell proliferation

All the three kinds of BCP granules had good cellular compatibility. From Calcein-AM/PI staining images (Fig. 2A), MC3T3 grew quite well on BCP-micro, BCP-nano and BCP-control with few dead cells (red), and apparent cell proliferation could be observed. The obtained BCP granules could also promote the spreading of MC3T3, the cells attached and spread well on the BCP granules after 2 days of culturing (Fig. 2A), as the

MC3T3 exhibited a typically spindle-shaped morphology, and abundant filopodia were outstretched to tightly grasp the crystal grains from SEM images. In addition, cells formed extensive cell-cell interactions from F-actin/DAPI staining after 3 days of culturing (Fig. 2A). These findings were consistent with the MTT results (Fig. 2B), as the quantity of cells on the three kinds of BCP granules increased remarkably with prolonging the culturing time. The results of protein adsorption (Fig. 2C) revealed that BCP-nano could adsorb more protein than BCP-control and BCP-micro, either for bovine serum albumin (BSA) or for fibronectin (FN), the protein adsorbing ability of BCP-control was relatively low among the three groups.

**Table 1**  
Summary of physicochemical data of BCP-micro, BCP-nano and BCP-control.

Samples	Grain size	Phase ratio	Porosity	Microporosity <sup>a</sup>	SSA
	(nm)	(HA/ β-TCP)	(%)	(%)	(m <sup>2</sup> g <sup>-1</sup> )
BCP-	503.9 ±	73.0/	69.85 ±	23.67 ± 1.05	0.850 ±
micro	105.6	27.0	1.05		0.054
BCP-nano	122.8 ±	69.2/	73.66 ±	33.29 ± 2.67	6.656 ±
	30.1	30.8	2.20		1.406
BCP-	652.9 ±	21.9/	77.71 ±	18.51 ± 1.69	0.594 ±
control	153.9	78.1	1.49		0.146

<sup>a</sup> Volume percentage of micropores smaller than 10 μm within the BCP granules.

**3.3. ALP staining and alizarin red S staining**

ALP staining and Alizarin Red S staining of MC3T3 cultured on BCP-micro, BCP-nano and BCP-control for the different culturing time were shown in Fig. 3. From the ALP staining (Fig. 3A), BCP-nano exhibited the darkest color among the three groups at day 4 and day 7, followed by BCP-micro, and the color was lightest in BCP-control. These observations were consistent with the semi-quantitative analysis of optimal density in Fig. 3B. The quantitative analysis of ALP activity was further carried out

and shown in Fig. 3C, which reinforced that BCP-nano owed relatively high ALP activity comparing with BCP-micro and BCP-control. Alizarin Red S staining (Fig. 3D) was implemented to evaluate the calcified nodules of MC3T3 after culturing for 7, 14 and 21 days. At day 7, all the three groups exhibited the light-dark of Alizarin Red S staining. With prolonging the culture time for 14 days and 21 days, apparent calcified nodules were observed in all the three groups, and BCP-micro and BCP-nano had relatively higher expressions than BCP-control (Fig. 3E).

**3.4. Immunofluorescent staining**

Immunofluorescent staining was carried out to evaluate the expressions of osteogenic markers, including BMP-2, Runx-2, COL-I, OCN and OPN, and exhibited in Fig. 4. All the three kinds of BCP granules could promote the secretions of these osteogenic proteins after 14 days of culturing. For the early osteogenic markers of BMP-2, Runx-2 and COL-I, BCP-nano owed the higher expressions than BCP-micro and BCP-control, while there was no significant difference in these expressions between BCP-micro and BCP-control. For the late osteogenic markers of OCN and OPN, the expressions were promoted by BCP-micro and BCP-nano, while BCP-control had relatively low expressions comparing with the other two groups. And BCP-nano had the highest expression of OCN among the three groups. These results clearly indicated that BCP-nano could also promote the expressions of osteogenesis-related proteins in MC3T3.

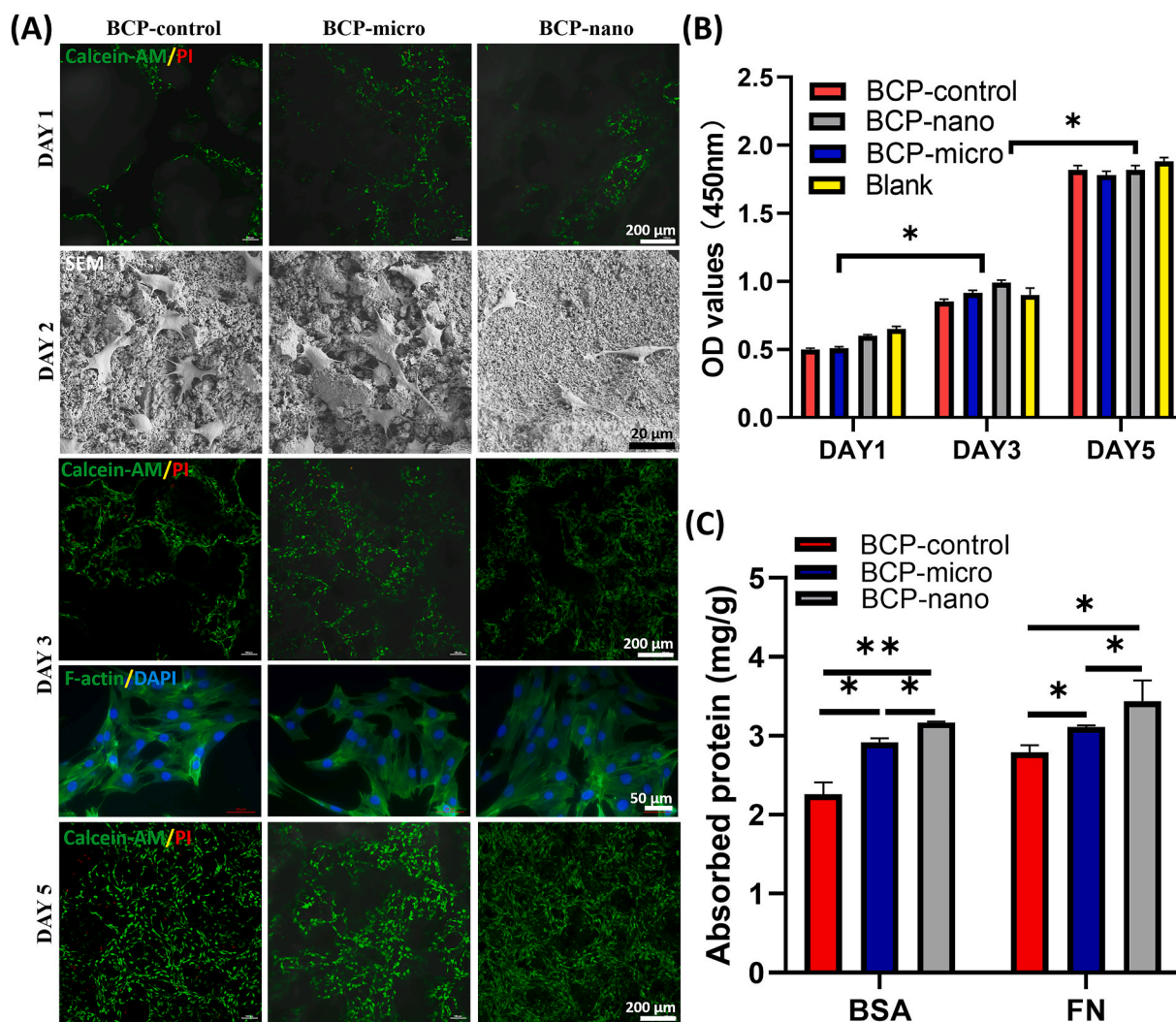


**Fig. 2.** (A) CLSM observations (Calcein-AM/PI and F-actin/DAPI) and SEM observations of MC3T3, (C) protein adsorption of BSA and FN on BCP-micro, BCP-nano and BCP-control. Values are expressed as the mean ± SD (n = 3), \* refers to p < 0.05, and \*\* refers to p < 0.01.

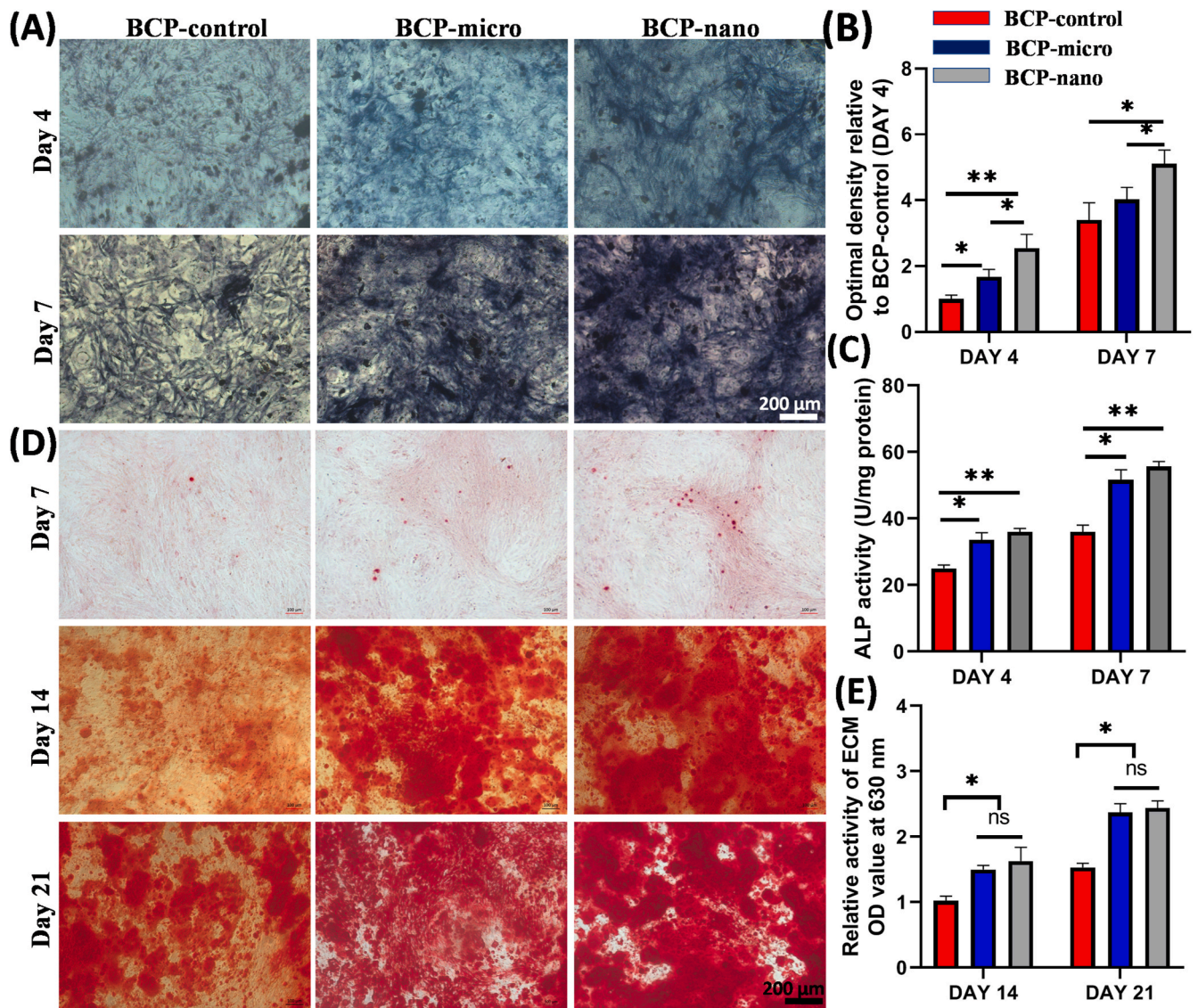


Fig. 3. (A) ALP staining, (B) semi-quantitative analysis and (C) ALP activity of MC3T3 culturing with medium extracted BCP-micro, BCP-nano and BCP-control for 4 and 7 days; (D) Alizarin Red S staining and (E) relative activity of ECM of MC3T3 culturing with medium extracted BCP-micro, BCP-nano and BCP-control for 7, 14 and 21 days. Values are expressed as the mean  $\pm$  SD ( $n = 3$ ), \* refers to  $p < 0.05$ , and \*\* refers to  $p < 0.01$ .

### 3.5. Osteogenic gene expression and protein secretion

The osteogenic gene expressions (*i.e.* *Runx-2*, *Osx*, *Col-I*, *Alp*, *Opn*, *Ocn*) of MC3T3 cultured on the three kinds of BCP granules were detected at 4, 7 and 14 days by qRT-PCR analysis and shown in Fig. 5. At day 4, the expressions of *Osx*, *Col-I*, *Alp*, *Opn* and *Ocn* of BCP-nano were highest among the three groups, while BCP-micro had the relatively low expressions of *Runx-2* and *Col-I* compared with BCP-nano and BCP-control, and BCP-control had the lower expressions of *Osx* and *Alp* than the other two groups. At day 7, BCP-nano had the highest expressions of *Alp* and *Opn*, and BCP-micro had the higher expressions of *Runx-2*, *Osx* and *Alp* than BCP-control, while the expressions of *Col-I* and *Ocn* in BCP-micro were lower than BCP-control and BCP-nano. At day 14, the expressions of all these osteogenic markers in BCP-nano were higher than BCP-control, and BCP-micro also had higher expressions of *Runx-2*, *Alp* and *Ocn* than BCP-control.

The osteogenesis-related markers of COL-I, BSP, OPN and OCN were further analyzed by Western blot (Fig. 5B). The results further confirmed the expressions of COL-I, BSP and OPN were up-regulated by BCP-nano, and BCP-micro had relatively higher expressions of BSP, OPN and OCN

than BCP-control, and the expressions of these markers in BCP-control was relatively lower than BCP-micro and BCP-nano (Fig. 5C). Overall, BCP-nano could promote the osteogenic differentiation of MC3T3 comparing with BCP-micro and BCP-control.

### 3.6. Manual palpation and X-ray evaluation

Results of fusion assessment by manual palpation in a blinded manner are presented in Table 2. The data indicated that BCP-nano possessed the highest manual palpation score ( $1.88 \pm 0.37$ ) and fusion efficiency (87.5%) among the three groups. The second was BCP-micro, it also had a relatively high manual palpation score ( $1.52 \pm 0.51$ ) and fast fusion rate (81.2%). The manual palpation score ( $1.38 \pm 0.42$ ) and fusion rate (68.7%) of BCP-control were relatively low.

*In vivo* X-ray scanning of each group was used to assess the fusing efficacy of PLF after implantation for 45 days (Fig. 6). It could be observed that the granules were evenly distributed in the transverse process space in all the three groups, and the material shadow was clearly visible without obvious absorption. Only a tiny amount of discontinuous callus could be seen between the transverse processes,

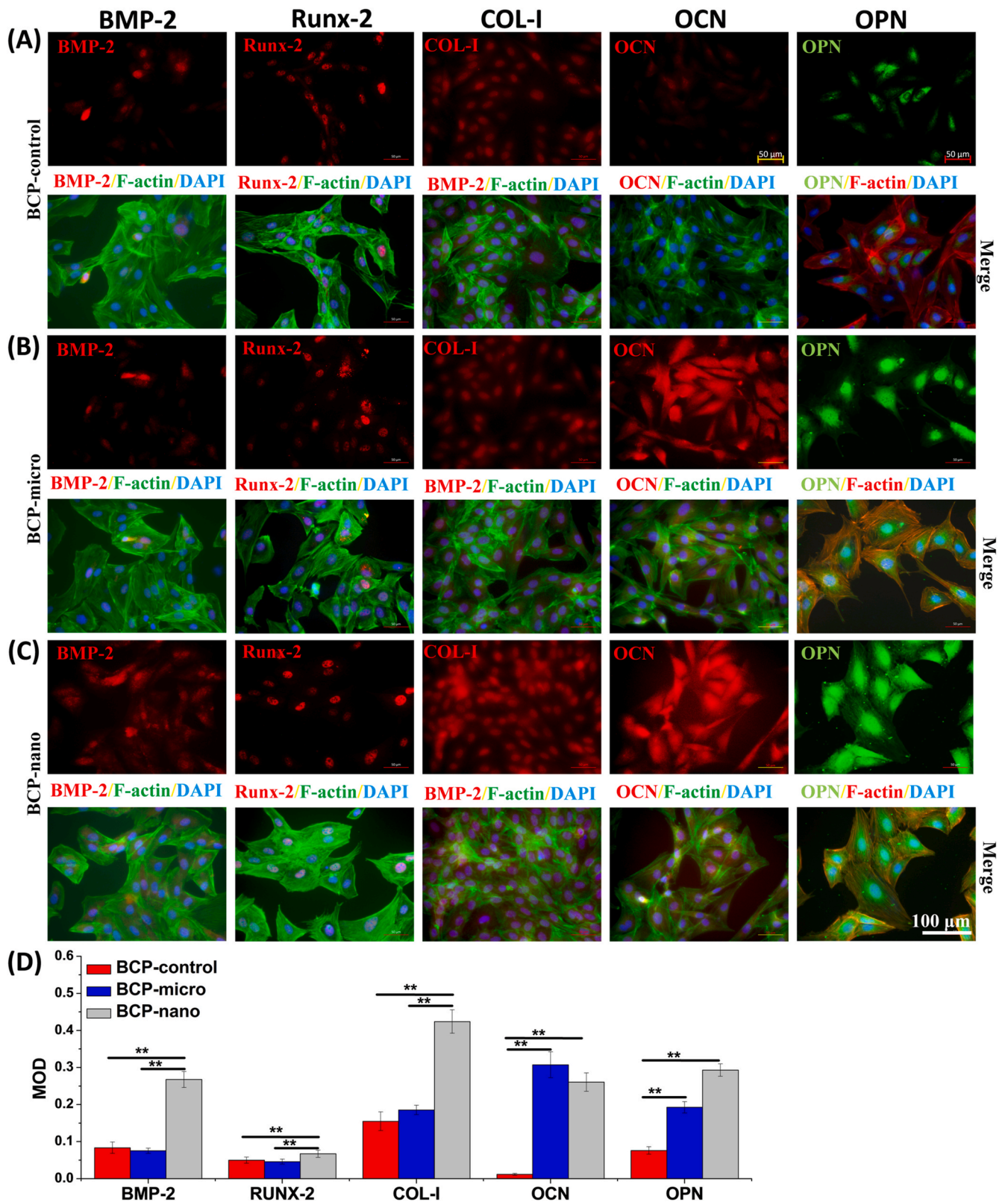
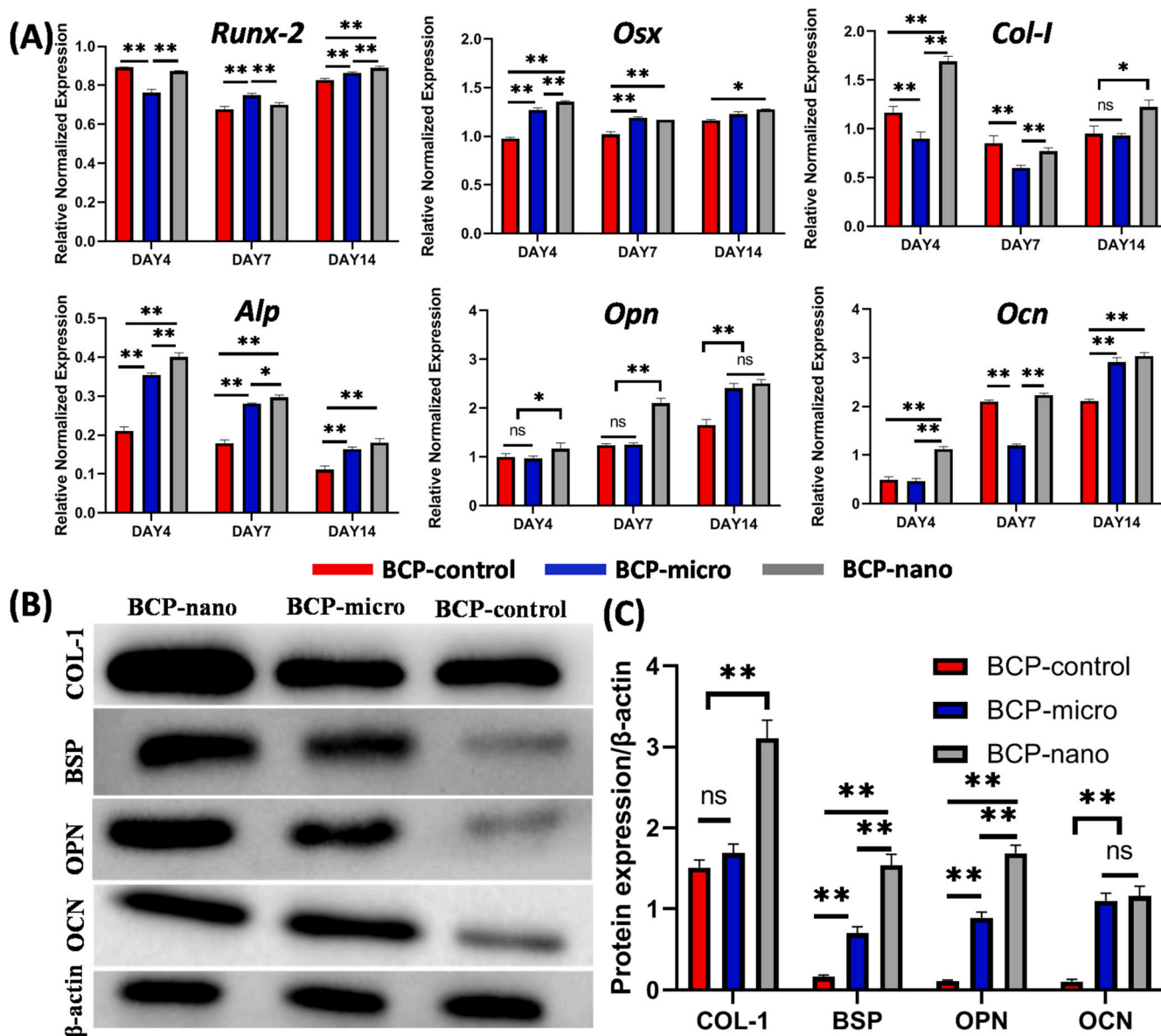


Fig. 4. Immunofluorescent staining and MOD values of BMP-2, Runx-2, COL-I, OCN, OPN in MC3T3 culturing on BCP-micro (A), BCP-nano (B) and BCP-control (C) for 14 days, and semi-quantification by optical density (D). For BMP-2, Runx-2, COL-I and OCN: red represents target protein, green represents cytoskeleton, blue represents cell nucleus; For OPN: green represents target protein, red represents cytoskeleton, blue represents cell nucleus. Values are expressed as the mean  $\pm$  SD ( $n = 3$ ), \* refers to  $p < 0.05$ , and \*\* refers to  $p < 0.01$ .



**Fig. 5.** (A) Expressions of osteogenic genes (*Runx-2*, *Osx*, *Col-1*, *Alp*, *Opn*, *Ocn*) in MC3T3 cultured on BCP-control, BCP-micro and BCP-nano for 4, 7, 14 days; (B) representative Western blot analysis for COL-1, BSP, OPN, OCN and  $\beta$ -actin protein expressions of the respective groups co-culturing with MC3T3 for 14 days; (C) the protein expression level of COL-1, BSP, OPN and OCN to the  $\beta$ -actin level. Values are expressed as the mean  $\pm$  SD (n = 3), \* refers to p < 0.05, and \*\* refers to p < 0.01.

**Table 2**

Evaluation of spinal fusion status 12 weeks after surgery with manual palpation and X-ray.

	BCP-control	BCP-micro	BCP-nano
Manual palpation (n/N) *	11/16	13/16	14/16
Manual palpation score	1.38 $\pm$ 0.42	1.52 $\pm$ 0.51	1.88 $\pm$ 0.37
X-ray evaluation (n/N)	10/16	12/16	14/16
X-ray score	4.0 $\pm$ 0.85	4.3 $\pm$ 0.92	4.7 $\pm$ 1.01
Fusion efficiency	68.8%	81.2%	87.5%

Note: N represented the number of evaluated samples, n represented the number of fused samples.

which was connected with the adjacent transverse processes to form bone bridge, but the solid fusion had not yet been achieved. After implanting for 90 days, all the three groups had a significantly increased callus between the transverse processes, and softening of the edges of the BCP granules were observed, which were connected with the adjacent

transverse processes to form bone bridges. And the BCP granules became indistinct and sparse compared with those at day 45, indicating partial absorption and degradation of materials after implantation for 90 days. The evaluations of spinal fusion based on X-ray at day 90 were also list in Table 2, and the fusion trend was similar to that of manual palpation. BCP-nano still had the highest fusion proportion (14/16) and fusion score (4.7  $\pm$  1.01) among the three groups. These results revealed that BCP-nano with spherical shape and nanocrystal could promote the poster-lateral spinal fusion comparing with BCP-micro and BCP-control.

### 3.7. Micro-CT analysis

Fusion between the transverse processes was also investigated by micro-CT analysis, a review of 3D models and three planes (coronal, sagittal and axial views) were reconstructed. Micro-CT images showed new bone bridging between adjacent transverse processes (marked by asterisks) in all the three groups (Fig. 7A). New bone tissue from the

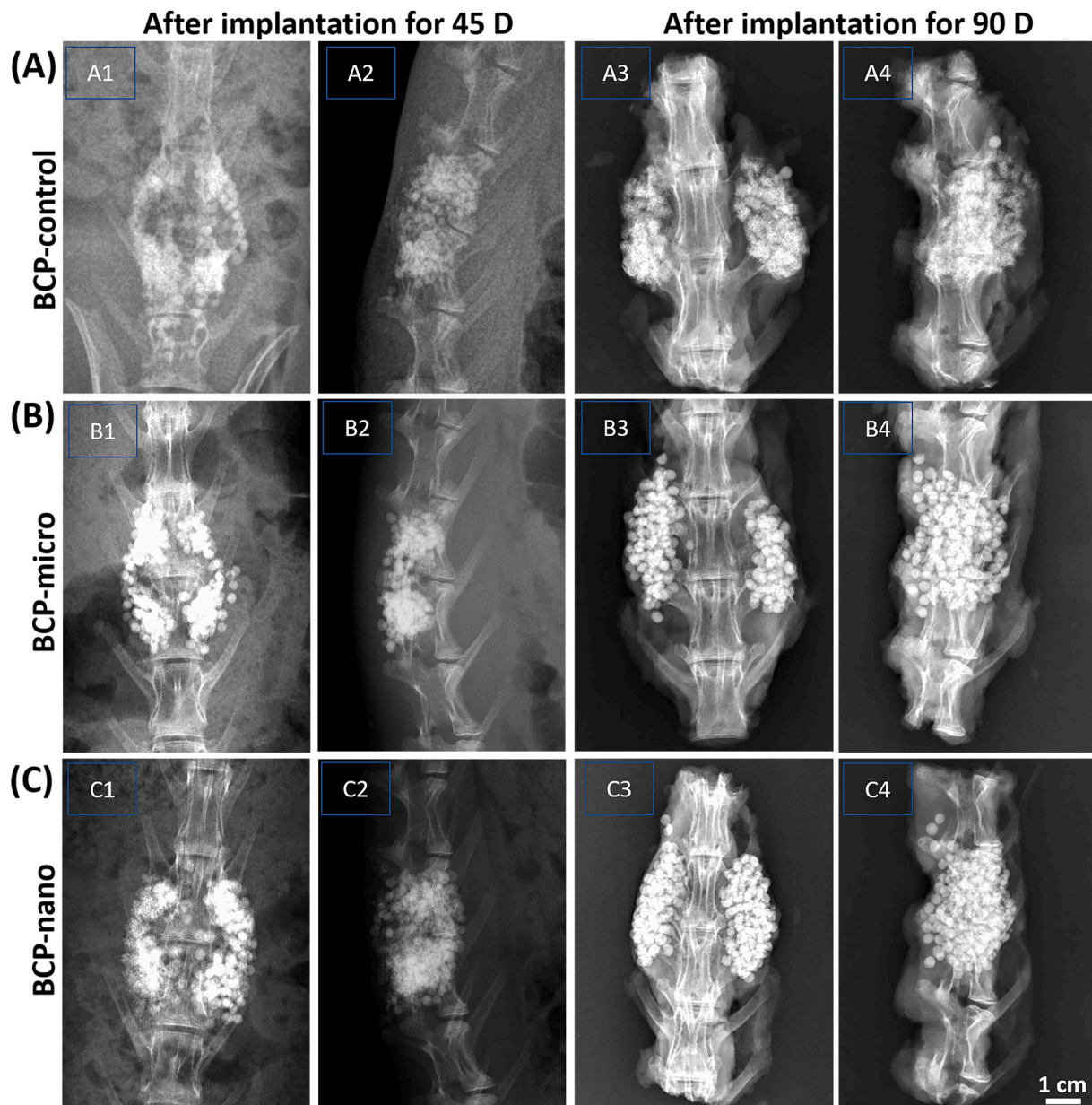
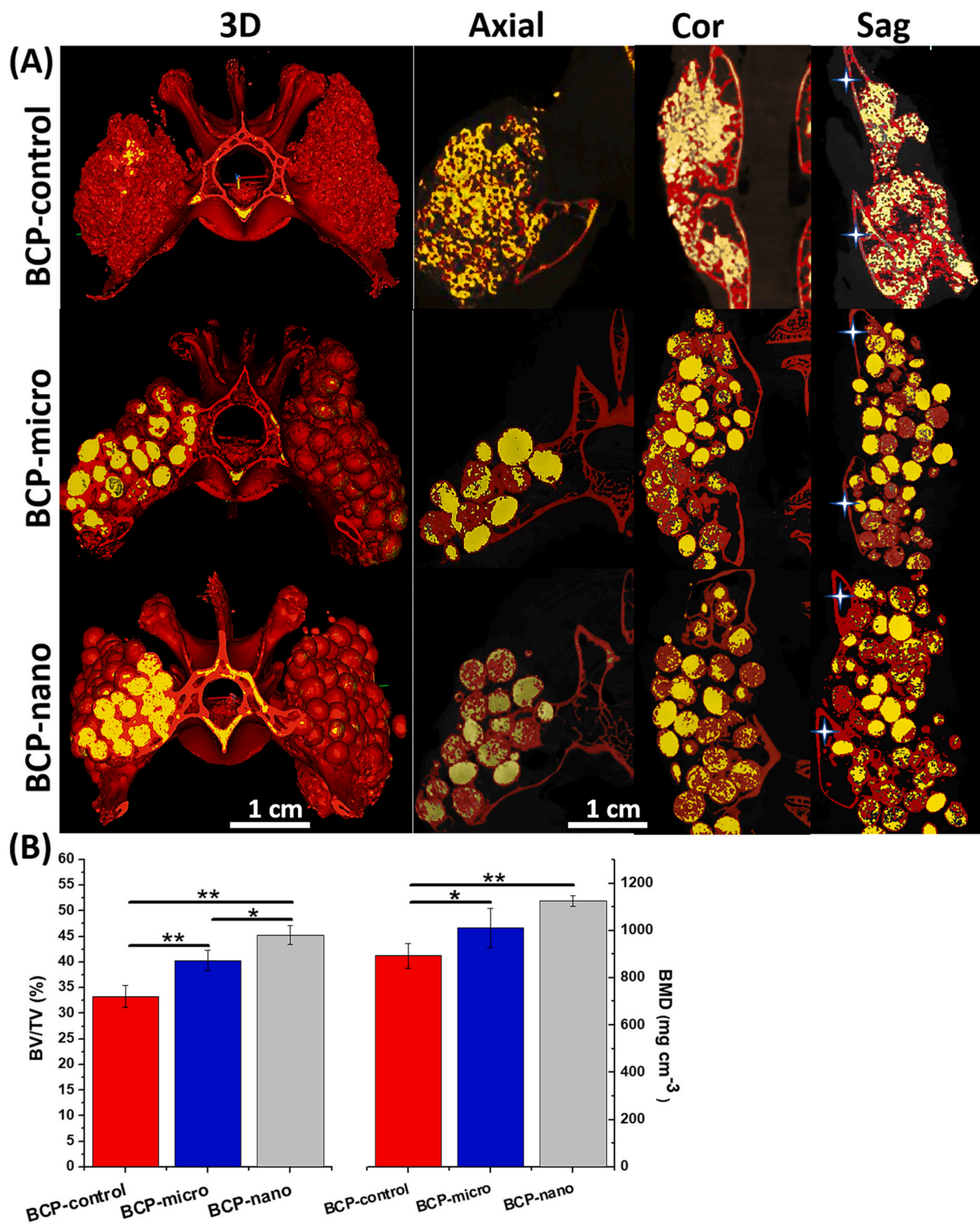


Fig. 6. X-ray images of one individual rabbit from each group as to track the healing stage of the defects implanted with BCP-control, BCP-micro and BCP-nano.

transverse process, articular process and adjacent lamina were closely connected with porous BCP granules, which formed a continuous bone bridging to the adjacent transverse processes and achieved posterolateral spinal fusion. In BCP-nano group, there was more trabecular-like bone surrounding the spherical granules and growing into their porous structure, a continuous bone bridge had been formed to connect the adjacent transverse processes. Moreover, the outlines of granules became indistinct, indicating the degradation occurred in BCP-nano group. The degradation was also observed in BCP-micro group, which was weaker than BCP-nano, and the amount of new bone was significantly less than BCP-nano. In BCP-control group, there were some gaps in the interface between granules and transverse process, indicating that the formation of new bone between granules and autogenous bone of transverse process was not complete. From the quantitative analysis of new bone formation in the defect sites (Fig. 7B), the bone volume fraction (BV/TV) followed the order BCP-nano > BCP-micro > BCP-control, and the bone mineral densities (BMD) of BCP-nano and BCP-micro were higher than BCP-control.

### 3.8. Histological analysis

The details of bone regeneration in the poster-lateral spinal environment after implantation for 90 days were shown in Fig. 8. From the histological overview (column 1), no inflammation was observed around the wound and many available spaces around spine were filled with new bone in all three groups. From higher magnification (column 1 and 2), it could be observed that many internal pores in BCP granules were filled with new bone. In addition, the amount of new bone in the region near the spine was more than that in the region far from the spine, due to the favorably osteoconductive environment near the spine. Moreover, the osteoinductivity phenomenon was also observed in BCP-micro and BCP-nano, which could be certified by the formation of new bone in the region far from the spine (column 3). Due to the relatively weak osteoinductivity of BCP-control, there was no new bone in the region far from the spine. By the quantitative statistics of new bone in available spaces of spine, the percentage of new bone in BCP-nano group was highest ( $16.83 \pm 1.02\%$ ), followed by BCP-micro group ( $15.59 \pm$



**Fig. 7.** Images and parameters rendered by micro-CT of BCP-control, BCP-micro and BCP-nano after implanting for 90 days: (A) representative 3D and tomographic images (coronal, axial and sagittal) demonstrating the current working threshold to segment the new bone (red) from the remaining materials (yellow), the asterisk represents the transverse process; (B) quantitative comparisons of the bone volume fraction (BV/TV) and bone mineral density (BMD). Values are expressed as the mean  $\pm$  SD ( $n = 3$ ), \* refers to  $p < 0.05$ , and \*\* refers to  $p < 0.01$ .

1.15%), BCP-control had the lowest value of  $12.78 \pm 2.35\%$ . Moreover, some degree of degradation was observed in BCP-nano, the outlines of granules became indistinct, and abundant inner pores were connected by the new bone.

### 3.9. Fluorochrome labeling analysis

From CLSM images (Fig. 9A), the mineralization and new bone formation in the three kinds of BCP ceramics were obviously labeled by calcein (green) and tetracycline (yellow). As exhibited in Fig. 9B, the area of calcein labeling in BCP-nano ( $12.23 \pm 1.41\%$ ) was the largest

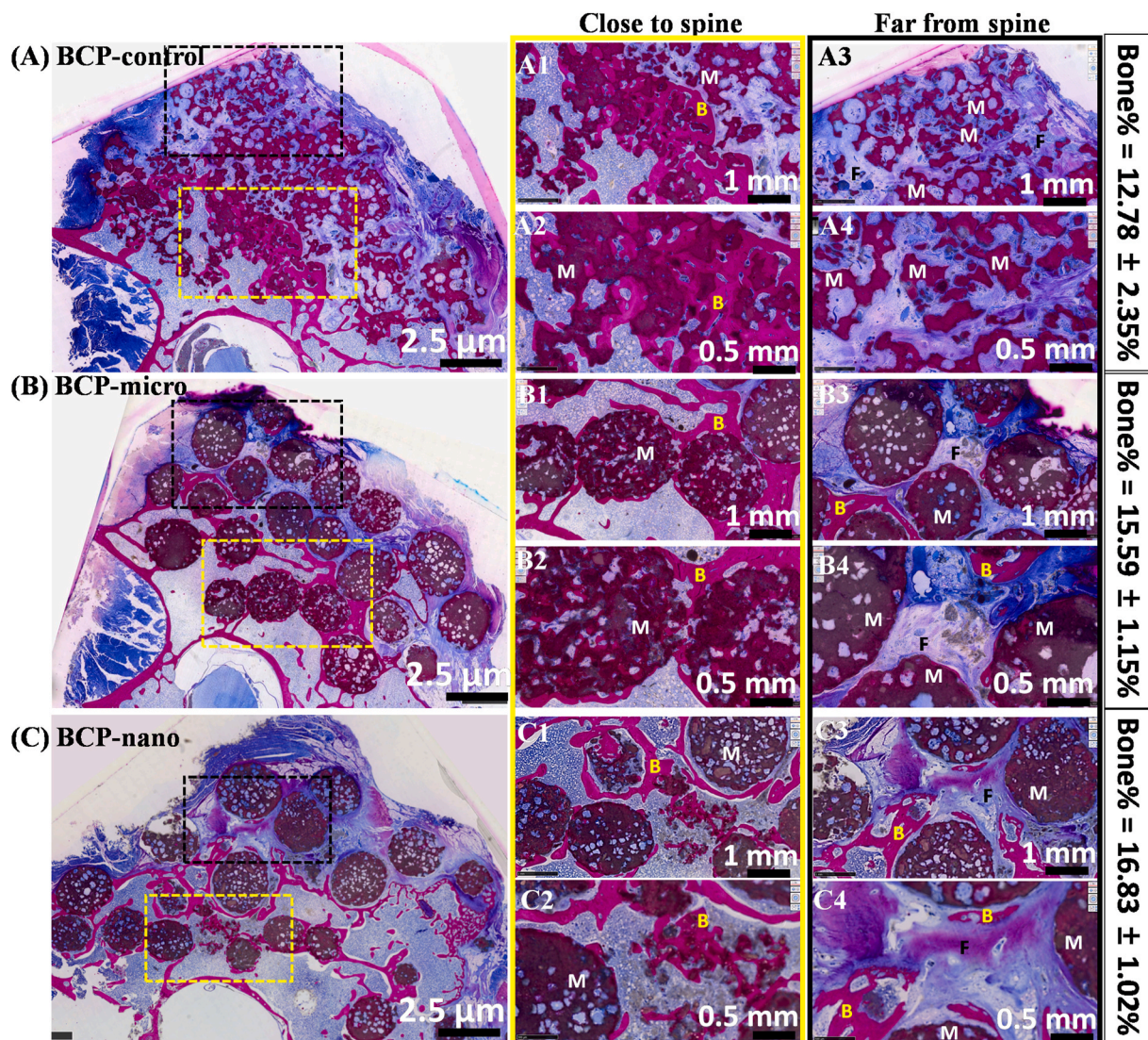


**Fig. 8.** Histological staining (un-decalcified sections stained with methylene-blue and basic magenta) and percentages of new bone in available spaces of spine treated with BCP-control, BCP-micro and BCP-nano after implantation for 90 days (M for Material, B for New Bone, F for fibrous tissue).

among the three groups, while the area of calcein labeling in BCP-micro ( $9.98 \pm 0.81\%$ ) was larger than BCP-control ( $3.23 \pm 0.85\%$ ). Similar phenomena were also observed from tetracycline labeling in the three groups. Quantitative analysis of the fluorescent marker intervals (Fig. 9C) revealed the bone apposition rate in BCP-nano ( $1.99 \pm 0.63 \mu\text{m}$  per day) was significantly higher than BCP-micro ( $1.38 \pm 0.28 \mu\text{m}$  per day) and BCP-control ( $0.89 \pm 0.22 \mu\text{m}$  per day), BCP-control had the lowest bone apposition rate among the three groups. Thus, these data indicated that BCP-nano with spherical shape and nanocrystal could promote the new bone formation and mineralization in PLF processes.

### 3.10. Biomechanical analysis

The process and schema of the three-point bending test were exhibited in Fig. 10. After implantation for 90 days, BCP-nano could bear the maximum bending load of  $202.55 \pm 14.80 \text{ N}$ , followed by BCP-micro of  $168.35 \pm 9.45 \text{ N}$ , and the maximum bending load of BCP-control was lowest ( $104.72 \pm 6.99 \text{ N}$ ). Similar tendency was also observed in the maximum bending stress of the three groups: BCP-nano ( $17.35 \pm 0.94 \text{ MPa}$ ) > BCP-micro ( $14.80 \pm 0.83 \text{ MPa}$ ) > BCP-control ( $9.21 \pm 0.62 \text{ MPa}$ ). Moreover, the bending stiffness of the fused spine was also characterized, BCP-nano had a higher bending stress ( $22.06 \pm$

$2.24 \text{ N mm}^{-1}$ ) than BCP-control ( $17.96 \pm 1.02 \text{ N mm}^{-1}$ ) and BCP-micro ( $11.17 \pm 0.75 \text{ N mm}^{-1}$ ). These results indicated that all the three groups had the spinal fusion to some extent, BCP-nano with spherical shape and nanocrystal could promote the fusion efficiency compared with BCP-control and BCP-micro.

## 4. Discussion

Posterolateral spinal fusion (PLF) is a common procedure in orthopedic surgery that is performed to fuse adjacent vertebrae to reduce symptoms related to spinal conditions [2,3]. As mentioned above, the osteogenic environment in the transverse processes of adjacent vertebrae is not so good. In order to improve the fuse efficiency of PLF procedures, some researchers proposed the use of rhBMP-2 in PLF, but the high doses of rhBMP-2 are high-cost and have security risks [5,40,41]. Some previous researches also reported the usage of Ca-P ceramics to support bone formation in the spine, but the fusion of such large segments is generally unsatisfactory and the new bone is merely observed in the regions close to the host bone bed on account of the limited osteoconductivity without osteoinductivity [42,43]. Therefore, developing osteoinductive Ca-P ceramics is the fundamental way to solve these problems. Intrinsic osteoinduction can bestow Ca-P ceramics with the

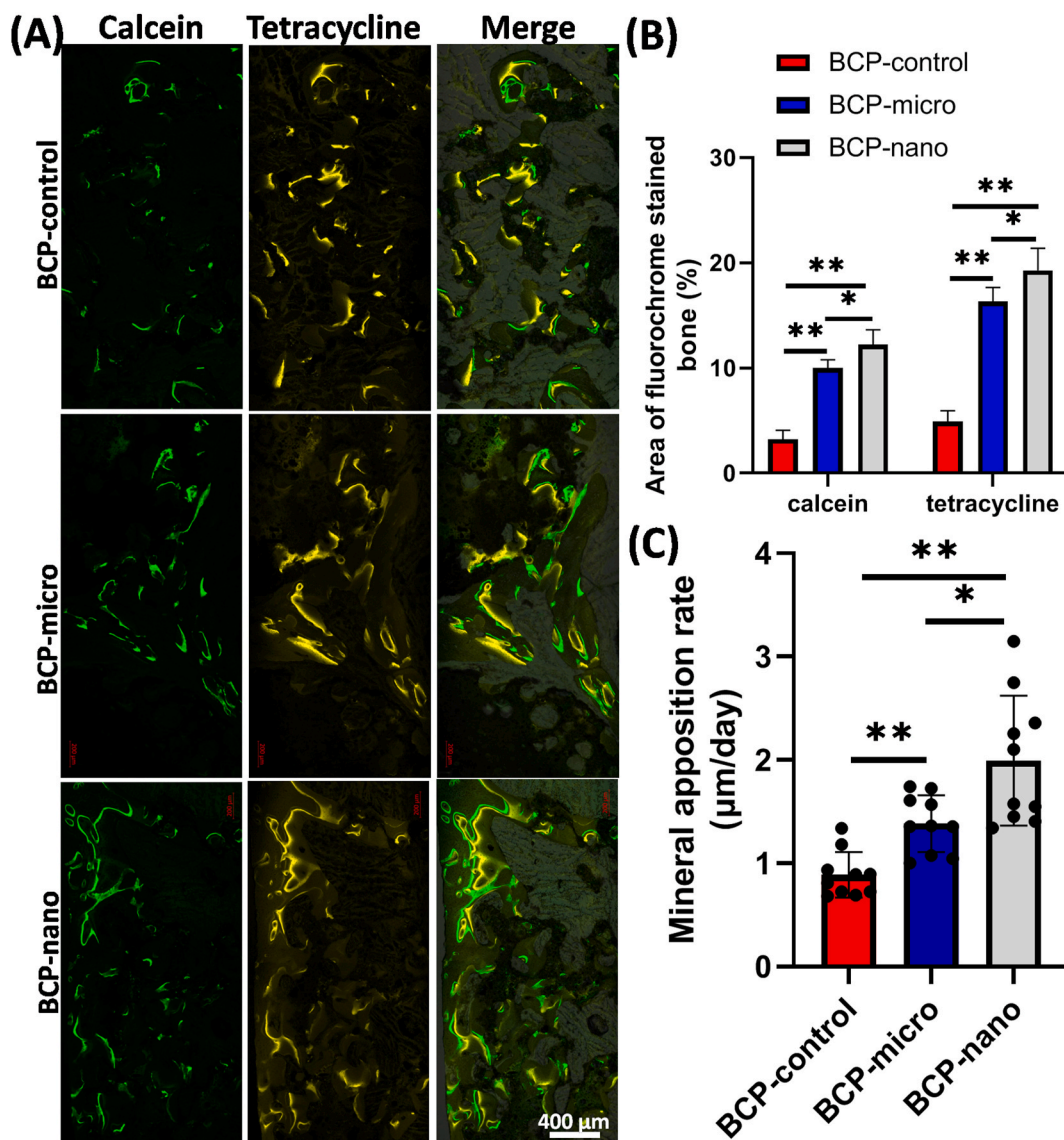


**Fig. 9.** Fluorochrome-labeling analysis of new bone formation and mineralization of post-surgery. (A) Column 1 (green) showed calcein-labeled newly formed bone at week 8, column 2 (yellow) showed tetracycline at week 10, row 3 represented merged images of the two fluorochromes with a light microscope. Scale bars: 400 μm. (B) Analysis of the fluorochrome-labeled new bone area and mineral apposition rate. Values are expressed as the mean ± SD, \* refers to  $p < 0.05$ , and \*\* refers to  $p < 0.01$ .

capacity to regulate cell behaviors, and promote the regeneration of the defected bone tissue, rather than adding any living cell or growth factor [15]. Previous studies have demonstrated that osteoinductive Ca-P ceramics have equal potential to autologous bone and rhBMP-2 to repair critical-sized defects in goat iliac model [1,5].

However, conventional Ca-P bioceramics still have some drawbacks in the bone regeneration of PLF. On the one hand, the most commonly used in PLF is generally irregular Ca-P ceramic granules [3,5,6,8], which are obtained by crushing ceramic blocks. However, these sharp angular granules may cause severe inflammatory reactions and attenuate bone formation reported by some studies [44,45]. On the other hand, the osteoinductivity of Ca-P bioceramics should be further improved to meet the requirements of regenerative medicine [19]. Therefore, it is urgent to fabricate a novel kind of Ca-P granules with regular shape and enhanced osteoinductivity. Our recent studies developed a convenient route to fabricate porous BCP ceramic spheres with nanocrystal by combining alginate gelatinizing with microwave hybrid sintering methods [26,29]. The obtained BCP nanoceramic spheres owned higher osteoinductivity than the submicro ones and commercial ones, and the

repairing of rabbit mandible critical-sized bone defect further certifies their excellent bone regenerative ability [26]. Based on the above discussion, the present study intends to further investigate the *in vitro* and *in vivo* biological performances of the porous BCP ceramic spheres with nanocrystal, especially their efficacy in guiding bone regeneration of rabbit posterolateral spinal fusion.

As mentioned above, the spherical shape and nanocrystal are two key factors to enhance bone regeneration in this study. As expected, BCP-micro and BCP-nano had well spherical shape with the diameter of about 2 μm, while, BCP-control had a sharply angular shape with the diameter of 2–4 μm. In addition, BCP-nano possessed the grain size of about 100 nm, yet BCP-micro and BCP-control had submicro- or micro-grain size of about 500–600 nm (Fig. 1). All the three kinds of BCP granules had interconnected pore structure (Fig. 1), which consisted of macropores (200–500 μm), interconnected pores (20–50 μm) and micropores (2–5 μm). And BCP-nano had significant more micropores than BCP-micro and BCP-control, which could provide larger specific surface area and surface roughness. In the study of Yuan HP et al., they demonstrated that the abundant micropores were corrected to the

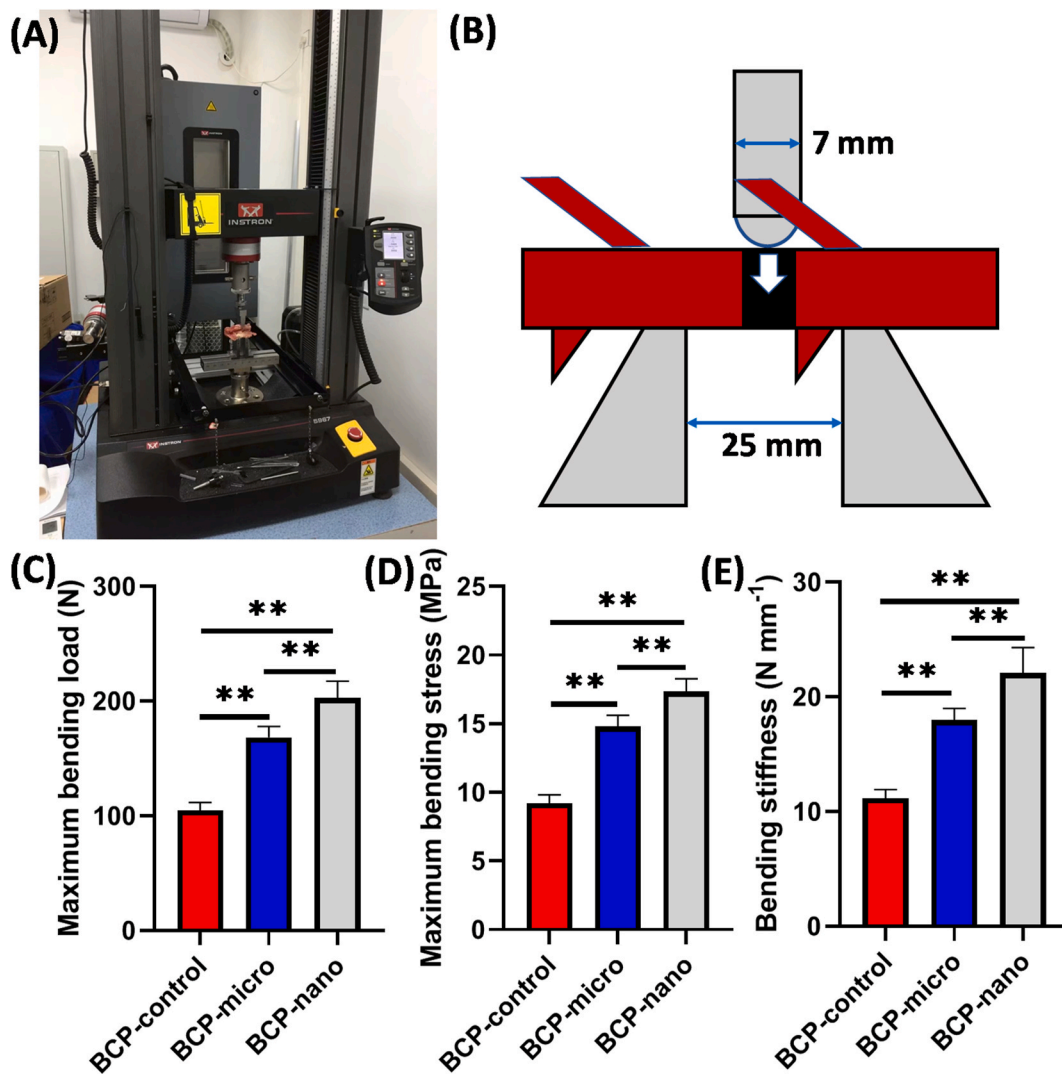


Fig. 10. Biomechanical testing: (A) three-point bending testing process; (B) the schema of three-point bending test; (C) maximum bending load; (D) maximum bending stress; (E) bending stiffness of the operative segment. Values are expressed as the mean  $\pm$  SD ( $n = 3$ ), \* refers to  $p < 0.05$ , and \*\* refers to  $p < 0.01$ .

propensity to stimulate osteogenic differentiation of stem cells *in vitro* and bone induction *in vivo* [1,46].

Moreover, the specific nanotopography could also well initiate the initial protein adsorption and regulate a cascade of gene activities of cells [47,48]. Due to the abundant micropores and large specific surface area, BCP-nano could adsorb more proteins (*i.e.* BSA and FN) than BCP-micro and BCP-control (Fig. 2C). It is known that protein adsorption is the first step in integrating implantations with tissue, which will affect even determine the biological performances of biomaterials. Moreover, the topography of Ca-P bioceramics could affect the conformation of the protein (*i.e.* BMP-2). Our previous study has proved that HA bioceramics with nanotopography could well maintain the secondary structure (*i.e.*  $\beta$ -sheet, random coil,  $\alpha$ -helix and  $\beta$ -turn) and conformation (*i.e.* tyrosine residue and tryptophan residue) of BMP-2 comparing with HA bioceramics with submicro- or micro-topography, which could facilitate cell adhesion and spreading, and activate the osteogenic differentiation of BMSCs [27]. Moreover, the strong adsorption affinity of BSA and FN of BCP-nano may mediate the expression of the integrin, which could involve in the transduction of “outside-in signaling” and then triggers the intracellular MAPK signaling cascade to induce the osteogenic differentiation of MSCs as proposed by previous study [31]. All the three kinds of groups had the well cellular biocompatibility, which could well promote the proliferation of MC3T3

(Fig. 2A–B). Compared with BCP-micro and BCP-control, BCP-nano could obviously promote ALP and calcified nodules expressions (Fig. 3), and exhibited higher expressions of BMP-2, Runx-2, COL-I, OCN, OPN from the immunofluorescent staining (Fig. 4). The nanotopography could also endow BCP bioceramics with enhanced osteogenic differentiation ability, BCP-nano exhibited significantly higher expressions of osteogenic markers (*i.e.* *Runx-2*, *Osx*, *Col-I*, *Alp*, *Opn* and *Ocn*) than BCP-micro and BCP-control (Fig. 5A). It should be noted that BCP-micro exhibited higher osteogenic differentiation ability than BCP-control, which might be partly attributed to the high microporosity of BCP-micro (list in Table 1). Apart from the above explanations, the nanocrystal of BCP-nano is more similar to the bony apatite than BCP-micro and BCP-control, which is more easily recognized by related proteins, cells and tissue and enhance their biological performances. These results could be further certified by WB analysis (Fig. 5B–C), BCP-nano had the highest protein expressions of COL-I, BSP, OPN and OCN among the three groups, and BCP-micro was more favorable to express these osteogenic markers than BCP-control, which indicated that both spherical shape and nanocrystal in BCP granules facilitated the osteogenic differentiation of MC3T3.

Posterolateral fusion in adult rabbits is a suitable model that provides insight into the *in vivo* performances of bone graft materials. As discussed above, the osteoinductivity of Ca-P bioceramics is a crucial factor

in determining their regenerative ability in PLF. Previous studies had certified that BCP granules with nanocrystal possessed higher osteoinductivity than BCP granules with microcrystal and BCP irregular granules, abundant connected new bone could be observed in BCP granules with nanocrystal after implantation in canine dorsal muscle for 45 days [16,26]. In the present study, osteoinductivity was also observed in BCP-micro and BCP-nano from the area far spine in Fig. 8, but BCP-control did not. Due to non-contacting with the transverse process, BCP granules were surrounding with muscle tissue, BCP-micro and BCP-nano should recruit the related proteins (*i.e.* BMP-2) and osteoprogenitor cells, such as mesenchymal stem cells (MSCs), and stimulate their differentiation in the osteogenic lineage [49–51]. Owing to the excellent osteoinductivity, the bone regeneration and fusing efficiency of BCP-micro and BCP-nano had significant advantages over BCP-control in PLF procedure. BCP-nano got relatively high scores of PLF fusion than BCP-micro and BCP-control in the manual palpation and X-ray evaluation, the scores of BCP-control were relatively low (Fig. 6 and Table 2). There was also more new bone in BCP-nano than BCP-micro and BCP-control. The adjacent transverse processes were connected by new forming bone in BCP-nano and BCP-micro, whereas some gaps in the interface between BCP-control granules and transverse process (Figs. 7 and 8). The fusion efficiency could also be reflected in the biomechanical tests, BCP-nano had a higher bending load, bending stress and bending stiffness than BCP-control and BCP-micro. Previous studies have indicated that a layer of bone-like apatite formed on the surfaces of Ca-P bioceramics can provide an excellent osteogenic microenvironment, which not only can adsorb many osteogenic proteins, but also can activate the osteogenic differentiation of cells [52–54]. The nanocrystal of BCP-nano is similar to the natural bony apatite, which could adsorb more proteins, facilitate cell adhesion, and be recognized by bone tissue easily, resulting in the acceleration of bone regeneration (Fig. 9). Recently, more and more researchers realize that immune responds also play an essential role in bone regeneration [55–57]. Osteoinductive BCP ceramics might regulate macrophage to secrete related chemokines *via* ERK signaling pathway, which would accelerate MSCs homing to facilitate bone formation [50]. In addition, the immune response of a biomaterial also determines its osteoinductive effect. Zhao Q et al. investigated the roles of macrophages and dendritic cells (DCs) during the osteoinduction of BCP scaffolds, and found that osteoinductive BCP directed M2 macrophage polarization and inhibited DC maturation, resulting in low T cell response and efficient osteogenesis [58]. Our previous work had been proved that HA bioceramics with nanotopography also had a significant influence on osteoclastogenesis, nanotopography markedly impaired osteoclastic formation and function compared to the ones with the submicron topography, which was further related to its osteoinductive capacity [25].

From the point of regenerative medicine, the ideal implants should be degraded gradually and replaced by the new tissue after accomplishing their mission of the initial scaffolds [19,59,60]. The degradation of scaffold should match with the growth rate of new bone, which is important to repair bone defects and reduce complications. Ca-P ceramics are generally considered bioabsorbable, but their degradation rate is usually low. Some studies attempted to improve the degradation ability by increasing the phase content of the highly soluble  $\beta$ -TCP phase, but the scope for adjustment is limited [28,61,62]. Moreover, only a proper proportion of HA/ $\beta$ -TCP in BCP bioceramics can have relatively high osteoinductivity, and higher  $\beta$ -TCP content does not mean stronger osteoinductivity. Therefore, the construction of nanotopography is a suitable way to endow BCP bioceramics with suitable degradation ability and superior osteoinductivity. After implantation for 90 days, BCP-nano exhibited higher degradability than BCP-micro and BCP-control, and their bone regenerative ability was also relatively strong (Fig. 8). Moreover, the uptake of calcium and phosphate ions from the cell culture medium (Fig. 1E) indicated that BCP-micro and BCP-nano facilitate the precipitation of apatite on their surfaces comparing with BCP-control. It is known that the precipitation of a new apatite occurs in

the vicinity of where the concentrations of calcium and phosphate ions have reached supersaturation. Following by the protein adsorption, osteogenic cells attachment and related stem cells differentiation, this apatite layer is reconstructed into bone-like tissue by osteoclasts [63–65]. In addition, there was no apparent change of major viscera organs of rabbits after implanting the three kinds of BCP granules, which further certified their good *in-vivo* biosafety, even though undergoing a relatively long period of implantation for 90 days (Fig. S3).

Nevertheless, this study has some limitations. First, the rabbit PLF model is limited in the anatomical and physiological differences between rabbit and human, because human PLF generally has an internal fixation system. Second, more extended implanting period beyond 90 days was not carried out, and the long-term evaluations of BCP-nano in the PLF fusion efficiency and biosafety need further study. The nice thing here is that another large animal experiment in a goat PLF model is in the process to further evaluate the bone regeneration of the BCP granules.

## 5. Conclusion

As discussed, it could be concluded that the present study provided the solid evidence of bone regeneration in a clinically relevant rabbit PLF model by employing osteoinductive BCP bioceramics. Due to the nanocrystal similar to natural bone apatite, BCP-nano was more conducive to protein adsorption and osteogenic differentiation of MC3T3 than BCP-control and BCP-micro. Further *in vivo* rabbit PLF procedures confirmed that nanotopography in BCP-nano might be responsible for the stronger bone regenerative ability than BCP-micro and BCP-control, owing to its relatively higher osteoinductivity. Although further long-term evaluations are required, it is believed that the porous BCP nanoceramic spheres hold great potential to become an alternative to standard bone grafts for clinical PLF applications.

## CRedit authorship contribution statement

**Xiangfeng Li:** Conceptualization, Methodology, Resources, Writing – original draft, Writing – review & editing, Funding acquisition. **Quan Zhou:** Investigation, Methodology, Validation. **Yonghao Wu:** Validation, Formal analysis. **Cong Feng:** Formal analysis. **Xi Yang:** Methodology, Supervision. **Linnan Wang:** Methodology, Supervision. **Yumei Xiao:** Supervision. **Kai Zhang:** Methodology, Resources. **Xiangdong Zhu:** Resources, Project administration, Writing – review & editing. **Limin Liu:** Supervision. **Yueming Song:** Resources, Project administration, Writing – review & editing. **Xingdong Zhang:** Conceptualization, Project administration, Supervision.

## Declaration of competing interest

The authors declare that they have no known competing financial interests or personal relationships that could have appeared to influence the work reported in this paper.

## Acknowledgements

This work was sponsored by the National Natural Science Foundation of China (52002256), Sichuan Science and Technology Innovation Team of China (2019JDTD0008), China Postdoctoral Innovation Talent Support program (BX20180204), China Postdoctoral Science Foundation (2018M643483), Sichuan University Postdoctoral Interdisciplinary Innovation Fund (0900904153024). The authors thank Ms. Jiao Lu, Ms. Lingzhu Yu, and Mr. Guolong Meng for their help for SEM and CLSM measurements. The authors would also like to thank Dr. Li Chen from Analytical & Testing Center of Sichuan University for her help with micro-CT.

## Appendix A. Supplementary data

Supplementary data to this article can be found online at <https://doi.org/10.1016/j.bioactmat.2021.10.006>.

## References

- [1] H. Yuan, H. Fernandes, P. Habibovic, J. De Boer, A.M.C. Barradas, A. De Ruiter, et al., Osteoinductive ceramics as a synthetic alternative to autologous bone grafting, *Proc. Natl. Acad. Sci. U.S.A.* 107 (31) (2010) 13614–13619, <https://doi.org/10.1073/pnas.1003600107>.
- [2] Y. Lu, M. Li, Z. Long, D. Yang, S. Guo, J. Li, et al., Collagen- $\beta$ -TCP composite as a bone-graft substitute for posterior spinal fusion in rabbit model: a comparison study, *Biomater. Mater.* 14 (4) (2019), <https://doi.org/10.1088/1748-605X/ab1caf>.
- [3] L.V. Dijk, D. Barbieri, F.B.-D. Groot, H. Yuan, R. Oliver, C. Christou, et al., Efficacy of a synthetic calcium phosphate with submicron surface topography as autograft extender in lapine posterolateral spinal fusion, *J. Biomed. Mater. Res. Part B* 107B (2019) 2080–2090, <https://doi.org/10.1002/jbm.b.34301>.
- [4] M. Djurasovic, S.D. Glassman, I.I. Dimar, J.M. Howard, K.R. Bratcher, L.Y. Carreon, Does fusion status correlate with patient outcomes in lumbar spinal fusion? *Spine* 36 (10) (2011) 58S–59S, <https://doi.org/10.1097/BRS.0b013e3181fde2c4>.
- [5] R. Duan, D. Barbieri, X. Luo, J. Weng, J.D. Bruijn, H. Yuan, Submicron-surface structured tricalcium phosphate ceramic enhances the bone regeneration in canine spine environment, *J. Orthop. Res.* 34 (11) (2016) 1865–1873, <https://doi.org/10.1002/jor.23201>.
- [6] M. Motomiya, M. Ito, M. Takahata, K. Kadoya, K. Irie, K. Abumi, et al., Effect of Hydroxyapatite porous characteristics on healing outcomes in rabbit posterolateral spinal fusion model, *Eur. Spine J.* 16 (12) (2007) 2215–2224, <https://doi.org/10.1007/s00586-007-0501-0>.
- [7] M.A. Plantz, S. Minardi, J.G. Lyons, A.C. Greene, E.L. Hsu, Osteoinductivity and biomechanical assessment of a 3D printed demineralized bone matrix-ceramic composite in a rat spine fusion model, *Acta Biomater.* 127 (11) (2021), <https://doi.org/10.1016/j.actbio.2021.03.060>.
- [8] L.A. van Dijk, R. Duan, X. Luo, D. Barbieri, M. Pelletier, C. Christou, et al., Biphasic calcium phosphate with submicron surface topography in an ovine model of instrumented posterolateral spinal fusion, *JOR Spine* 1 (4) (2018), <https://doi.org/10.1002/jsp2.1039>.
- [9] E.J. Carragee, G.C. Comer, M.W. Smith, Local bone graft harvesting and volumes in posterolateral lumbar fusion: a technical report, *Spine J.* 11 (6) (2011) 540–544, <https://doi.org/10.1016/j.spinee.2011.02.014>.
- [10] G. Grabowski, C.A. Cornett, Bone graft and bone graft substitutes in spine surgery: current concepts and controversies, *J. Am. Acad. Orthop. Surg.* 21 (1) (2013) 51–60, <https://doi.org/10.5435/JAAOS-21-01-51>.
- [11] A. Kadam, P.W. Millhouse, C.K. Kepler, K.E. Radcliff, A. Vaccaro, Bone substitutes and expanders in Spine Surgery: a review of their fusion efficacies, *Internet J. Spine Surg.* 10 (2016) 33, <https://doi.org/10.14444/3033>, 2016.
- [12] J.R. Dimar, S.D. Glassman, K.J. Burkus, L.Y. Carreon, Clinical outcomes and fusion success at 2 years of single-level instrumented posterolateral fusions with recombinant human bone morphogenetic protein-2/compression resistant matrix versus iliac crest bone graft, *Spine* 31 (22) (2006) 2534–2539, <https://doi.org/10.1097/01.brs.0000240715.78657.81>.
- [13] I.I. John, S.D. Glassman, J.K. Burkus, P.W. Pryor, J.W. Hardacker, L.Y. Carreon, Two-year fusion and clinical outcomes in 224 patients treated with a single-level instrumented posterolateral fusion with iliac crest bone graft, *Spine J.* 9 (11) (2009) 880–885, <https://doi.org/10.1016/j.spinee.2009.03.013>.
- [14] C. Feng, Y. Wu, Q. Cao, X. Li, X. Zhang, Effect of hydrothermal Media on the in-situ whisker growth on biphasic calcium phosphate ceramics, *Int. J. Nanomed.* 16 (2021) 147–159, <https://doi.org/10.2147/IJN.S280130>.
- [15] Z. Tang, X. Li, Y. Tan, H. Fan, X. Zhang, The material and biological characteristics of osteoinductive calcium phosphate ceramics, *Regen. Biomater.* 5 (1) (2018) 43–59, <https://doi.org/10.1093/rb/rbx024>.
- [16] Y. Hong, H. Fan, B. Li, B. Guo, M. Liu, X. Zhang, Fabrication, biological effects, and medical applications of calcium phosphate nanoceramics, *Mater. Sci. Eng. R Rep.* 70 (3–6) (2010) 225–242, <https://doi.org/10.1016/j.mser.2010.06.010>.
- [17] M. Bohner, R.J. Miron, A proposed mechanism for material-induced heterotopic ossification, *Mater. Today* 22 (2019) 132–141, <https://doi.org/10.1016/j.mattod.2018.10.036>.
- [18] X. Zhang, D. Williams, *Definitions of Biomaterials for the Twenty-First Century*, Elsevier, Amsterdam, 2019.
- [19] C. Zhou, X. Li, J. Cheng, H. Fan, X. Zhang, *Bioactive Ceramics and Metals for Regenerative Engineering*, Regenerative Engineering: Advanced Materials Science Principles, CRC Press, Boca Raton, 2018, pp. 31–43.
- [20] J.D. Pasteris, B. Wopenka, E. Valsami-Jones, Bone and tooth mineralization: why apatite? *Elements* 4 (2) (2008) 97–104, <https://doi.org/10.2113/GSELEMENTS.4.2.97>.
- [21] Z. Li, T. Du, C. Ruan, X. Niu, Bioinspired mineralized collagen scaffolds for bone tissue engineering, *Bioact. Mater.* 6 (5) (2021) 1491–1511, <https://doi.org/10.1016/j.bioactmat.2020.11.004>.
- [22] B. Li, X. Chen, B. Guo, X. Wang, H. Fan, X. Zhang, Fabrication and cellular biocompatibility of porous carbonated biphasic calcium phosphate ceramics with a nanostructure, *Acta Biomater.* 5 (1) (2009) 134–143, <https://doi.org/10.1016/j.actbio.2008.07.035>.
- [23] S. Bose, S. Dasgupta, S. Tarafder, A. Bandyopadhyay, Microwave-processed nanocrystalline hydroxyapatite: simultaneous enhancement of mechanical and biological properties, *Acta Biomater.* 6 (9) (2010) 3782–3790, <https://doi.org/10.1016/j.actbio.2010.03.016>.
- [24] J. Wang, L.L. Shaw, Nanocrystalline hydroxyapatite with simultaneous enhancements in hardness and toughness, *Biomaterials* 30 (34) (2009) 6565–6572, <https://doi.org/10.1016/j.biomaterials.2009.08.048>.
- [25] F. Chen, M. Wang, J. Wang, X. Chen, X. Li, Y. Xiao, et al., Effects of hydroxyapatite surface nano/micro-structure on osteoclast formation and activity, *J. Mat. Chem. B* 7 (47) (2019) 7574–7587, <https://doi.org/10.1039/C9TB01204D>.
- [26] X. Li, T. Song, X. Chen, M. Wang, X. Yang, Y. Xiao, et al., Osteoinductivity of porous biphasic calcium phosphate ceramic spheres with nanocrystalline and their efficacy in guiding bone regeneration, *ACS Appl. Mater. Interfaces* 11 (4) (2019) 3722–3736, <https://doi.org/10.1021/acsami.8b18525>.
- [27] X. Li, M. Liu, F. Chen, Y. Wang, M. Wang, X. Chen, et al., Design of hydroxyapatite bioceramics with micro-/nano-topographies to regulate the osteogenic activities of bone morphogenetic protein-2 and bone marrow stromal cells, *Nanoscale* 12 (13) (2020) 7284–7300, <https://doi.org/10.1039/C9NR10561A>.
- [28] S. Samavedi, A.R. Whittington, A.S. Goldstein, Calcium phosphate ceramics in bone tissue engineering: a review of properties and their influence on cell behavior, *Acta Biomater.* 9 (9) (2013) 8037–8045, <https://doi.org/10.1016/j.actbio.2013.06.014>.
- [29] X. Li, M. Wang, Y. Deng, X. Chen, Y. Xiao, X. Zhang, Fabrication and properties of Ca-P bioceramic spherical granules with interconnected porous structure, *ACS Biomater. Sci. Eng.* 3 (8) (2017) 1557–1566, <https://doi.org/10.1021/acsbomaterials.7b00232>.
- [30] Z. Luo, X. Chen, M. Liu, Y. Wang, D. Li, X. Li, et al., The controlled release of a novel thiolated icariin for enhanced osteoporotic bone regeneration, *Mater. Des.* 200 (2) (2021), <https://doi.org/10.1016/j.matdes.2021.109468>.
- [31] X. Chen, J. Wang, Y. Chen, H. Cai, X. Zhang, X. Zhu, et al., Roles of calcium phosphate-mediated integrin expression and MAPK signaling pathways in the osteoblastic differentiation of mesenchymal stem cells, *J. Mat. Chem. B* 4 (13) (2016) 2280–2289, <https://doi.org/10.1039/C6TB00349D>.
- [32] L.Y. Dai, L.S. Jiang, Single-level instrumented posterolateral fusion of lumbar spine with  $\beta$ -tricalcium phosphate versus autograft: a prospective, randomized study with 3-year follow-up, *Spine* 33 (12) (2008) 1299–1304, <https://doi.org/10.1097/BRS.0b013e3181732a8e>.
- [33] S.D. Boden, J.H. Schimandle, W.C. Hutton, An experimental lumbar intertransverse process spinal fusion model. Radiographic, histologic, and biomechanical healing characteristics, *Spine* 20 (4) (1995) 412–420, <https://doi.org/10.1097/00007632-199502001-00003>.
- [34] X. Zhuo, C. Li, B. Li, Z. Li, H. Lv, J. Huang, et al., Effects of combined magnetic fields (CMF) treatment and nano-hydroxyapatite (HA) coating on porous biphasic calcium phosphate (BCP) bone graft in rabbit spinal fusion model, *Spine* 43 (11) (2017), <https://doi.org/10.1097/BRS.0000000000002463>, E625–E633.
- [35] R. Zhao, S. Chen, W. Zhao, L. Yang, B. Yuan, V.S. Ioan, et al., A bioceramic scaffold composed of strontium-doped three-dimensional hydroxyapatite whiskers for enhanced bone regeneration in osteoporotic defects, *Theranostics* 10 (4) (2020) 1572–1589, <https://doi.org/10.7150/tno.40103>.
- [36] Y. Zhu, K. Zhang, R. Zhao, X. Ye, X. Chen, Z. Xiao, et al., Bone regeneration with micro/nano hybrid-structured biphasic calcium phosphate bioceramics at segmental bone defect and the induced immunoregulation of MSCs, *Biomaterials* 147 (2017) 133–144, <https://doi.org/10.1016/j.biomaterials.2017.09.018>.
- [37] D. Zhou, Z. Zhang, J. He, S. Zhu, S. Wang, W. Zhang, et al., Repairing critical-sized calvarial defects with BMSCs modified by a constitutively active form of hypoxia-inducible factor-1 $\alpha$  and a phosphate cement scaffold, *Biomaterials* 32 (36) (2011) 9707–9718, <https://doi.org/10.1016/j.biomaterials.2011.09.005>.
- [38] P.A. Glazer, M.R. Heilmann, J.C. Lotz, D.S. Bradford, Use of electromagnetic fields in a spinal fusion, A rabbit model, *Spine* 22 (20) (1997) 2351–2356, <https://doi.org/10.1097/00007632-199710150-00007>.
- [39] X. Li, Y. Deng, M. Wang, X. Chen, Y. Xiao, X. Zhang, Stabilization of Ca-deficient hydroxyapatite in biphasic calcium phosphate ceramics by adding alginate to enhance their biological performances, *J. Mat. Chem. B* 6 (1) (2018) 84–97, <https://doi.org/10.1039/C7TB02620J>.
- [40] J. Even, M. Eskander, J. Kang, Bone morphogenetic protein in spine surgery: current and future uses, *J. Am. Acad. Orthop. Surg.* 20 (9) (2012) 547–552, <https://doi.org/10.5435/JAAOS-20-09-547>.
- [41] C.A. Tannoury, H.S. An, Complications with the use of bone morphogenetic protein 2 (BMP-2) in spine surgery, *Spine J.* 14 (3) (2014) 552–559, <https://doi.org/10.1016/j.spinee.2013.08.060>.
- [42] M. Miyazaki, H. Tsumura, J.C. Wang, A. Alanay, An update on bone substitutes for spinal fusion, *Eur. Spine J.* 18 (6) (2009) 783–799, <https://doi.org/10.1007/s00586-009-0924-x>.
- [43] N.K. Acharya, R.J. Kumar, H.K. Varma, V.K. Menon, Hydroxyapatite-bioactive glass ceramic composite as stand-alone graft substitute for posterolateral fusion of lumbar spine: a prospective, matched, and controlled study, *J. Spinal Disord. Tech.* 21 (2) (2008) 106–111, <https://doi.org/10.1097/bsd.0b013e31805fea1f>.
- [44] C. Ribeiro, C. Barrias, M. Barbosa, Preparation and characterisation of calcium-phosphate porous microspheres with a uniform size for biomedical applications, *J. Mater. Sci. Mater. Med.* 17 (5) (2006) 455–463, <https://doi.org/10.1007/s10856-006-8473-x>.
- [45] D.J. Misiak, J.N. Kent, R.F. Carr, Soft tissue responses to hydroxylapatite particles of different shapes, *J. Oral Maxillofac. Surg.* 42 (3) (1984) 150–160, [https://doi.org/10.1016/S0278-2391\(84\)80025-7](https://doi.org/10.1016/S0278-2391(84)80025-7).
- [46] A. Barradas, H. Yuan, C. Blitterswijk, P. Habibovic, Osteoinductive biomaterials: current knowledge of properties, experimental models and biological mechanisms, *Eur. Cell. Mater.* 21 (2011) 407–429, <https://doi.org/10.22203/ecm.v021a31>.

- [47] A.W. Xu, Y. Ma, Biomimetic mineralization, *J. Mater. Chem.* 17 (5) (2007) 415–449, <https://doi.org/10.1039/b611918m>.
- [48] N.C. Seeman, A.M. Belcher, Emulating biology: building nanostructures from the bottom up, *Proc. Natl. Acad. Sci. U.S.A.* 99 (2) (2002) 6451–6455, <https://doi.org/10.1073/pnas.221458298>, Suppl. 2.
- [49] Y. Deng, M. Liu, X. Chen, M. Wang, X. Li, Y. Xiao, et al., Enhanced osteoinductivity of porous biphasic calcium phosphate ceramic beads with high content of strontium incorporated calcium deficient hydroxyapatite, *J. Mat. Chem. B* 6 (41) (2018) 6572–6584, <https://doi.org/10.1039/C8TB01637B>.
- [50] M. Wang, F. Chen, J. Wang, X. Chen, J. Liang, X. Yang, et al., Calcium phosphate altered the cytokine secretion of macrophages and influenced the homing of mesenchymal stem cells, *J. Mat. Chem. B* 6 (29) (2018) 4765–4774, <https://doi.org/10.1039/C8TB01201F>.
- [51] Z. Tang, Z. Wang, F. Qing, Y. Ni, Y. Fan, Y. Tan, et al., Bone morphogenetic protein Smads signaling in mesenchymal stem cells affected by osteoinductive calcium phosphate ceramics, *J. Biomed. Mater. Res.* 103 (3) (2015) 1001–1010, <https://doi.org/10.1002/jbm.a.35242>.
- [52] H. Wang, W. Zhi, X. Lu, X. Li, K. Duan, R. Duan, et al., Comparative studies on ectopic bone formation in porous hydroxyapatite scaffolds with complementary pore structures, *Acta Biomater.* 9 (9) (2013) 8413–8421, <https://doi.org/10.1016/j.actbio.2013.05.026>.
- [53] L. Xiong, L. Yang, Theoretical analysis of calcium phosphate precipitation in simulated body fluid, *Biomaterials* 26 (10) (2005) 1097–1108, <https://doi.org/10.1016/j.biomaterials.2004.05.034>.
- [54] H. Fan, T. Ikoma, J. Tanaka, X. Zhang, Surface structural biomimetics and the osteoinduction of calcium phosphate biomaterials, *J. Nanosci. Nanotechnol.* 7 (3) (2007) 808–813, <https://doi.org/10.1166/jnn.2007.501>.
- [55] Q. Zhao, M. Shi, C. Yin, Z. Zhao, J. Zhang, J. Wang, et al., Dual-wavelength photosensitive nano-in-micro scaffold regulates innate and adaptive immune responses for osteogenesis, *Nano-Micro Lett.* 13 (1) (2021), <https://doi.org/10.1007/s40820-020-00540-z>.
- [56] R. Sridharan, A.R. Cameron, D.J. Kelly, C.J. Kearney, F.J. O'Brien, Biomaterial based modulation of macrophage polarization: a review and suggested design principles, *Mater. Today* 18 (6) (2015) 313–325, <https://doi.org/10.1016/j.mattod.2015.01.019>.
- [57] Q. Fan, J. Bai, H. Shan, Z. Fei, C. Wang, Implantable blood clot loaded with BMP-2 for regulation of osteoimmunology and enhancement of bone repair, *Bioact. Mater.* 6 (11) (2021) 4014–4026, <https://doi.org/10.1016/j.bioactmat.2021.04.008>.
- [58] Q. Zhao, M. Shi, C. Yin, Z. Zhao, J. Zhang, J. Wang, et al., Dual-wavelength photosensitive nano-in-micro scaffold regulates innate and adaptive immune responses for osteogenesis, *Nano-Micro Lett.* 13 (1) (2021) 28, <https://doi.org/10.1007/s40820-020-00540-z>.
- [59] J. Chang, X. Zhang, K. Dai, *Bioactive Materials for Bone Regeneration*, Academic Press, San Diego, 2020.
- [60] W. Wang, K. Yeung, Bone grafts and biomaterials substitutes for bone defect repair: a review, *Bioact. Mater.* 2 (4) (2017) 224–247, <https://doi.org/10.1016/j.bioactmat.2017.05.007>.
- [61] X. Zhu, H. Zhang, H. Fan, L. Wei, X. Zhang, Effect of phase composition and microstructure of calcium phosphate ceramic particles on protein adsorption, *Acta Biomater.* 6 (4) (2010) 1536–1541, <https://doi.org/10.1016/j.actbio.2009.10.032>.
- [62] H.P. Yuan, M.V.D. Doel, L.I. Shi Hong, C.A.V. Blitterswijk, K.D. Groot, J.D. D. Bruijn, A comparison of the osteoinductive potential of two calcium phosphate ceramics implanted intramuscularly in goats, *J. Mater. Sci. Mater. Med.* 13 (12) (2002) 1271–1275, <https://doi.org/10.1023/a:1021191432366>.
- [63] T. Kokubo, H. Takadama, How useful is SBF in predicting in vivo bone bioactivity? *Biomaterials* 27 (15) (2006) 2907–2915, <https://doi.org/10.1016/j.biomaterials.2006.01.017>.
- [64] H. Wang, W. Zhi, X. Lu, X. Li, K. Duan, R. Duan, et al., Comparative studies on ectopic bone formation in porous hydroxyapatite scaffolds with complementary pore structures, *Acta Biomater.* 9 (9) (2013) 8413–8421, <https://doi.org/10.1016/j.actbio.2013.05.026>.
- [65] D.L. Nihouannen, G. Daculsi, A. Saffarzadeh, O. Gauthier, S. Delplace, P. Pilet, et al., Ectopic bone formation by microporous calcium phosphate ceramic particles in sheep muscles, *Bone* 36 (6) (2005) 1086–1093, <https://doi.org/10.1016/j.bone.2005.02.017>.